

# Highly Enhanced Adsorption For The Removal of Hg (II) From Aqueous Solution By Co-Polymerized Al<sub>2</sub>O<sub>3</sub> Nanocomposites Fabricated By Improved Sol-Gel Combustion Route: Synthesis, Adsorption Kinetics & Isotherm Modelling

Hesham H. El-Feky (✉ [hesham.elfeky@fsc.bu.edu.eg](mailto:hesham.elfeky@fsc.bu.edu.eg))

Benha University <https://orcid.org/0000-0002-8276-2222>

Alaa S. Amin

Benha University

Mostafa Y. Nassar

Benha University

---

## Research Article

**Keywords:** polymer, nanocomposites, combustion, Mercury and adsorption

**Posted Date:** September 9th, 2021

**DOI:** <https://doi.org/10.21203/rs.3.rs-884600/v1>

**License:**  This work is licensed under a Creative Commons Attribution 4.0 International License.

[Read Full License](#)

---

**Highly enhanced adsorption for the removal of Hg (II) from aqueous solution by co-polymerized Al<sub>2</sub>O<sub>3</sub> nanocomposites fabricated by improved sol-gel combustion route: Synthesis, adsorption kinetics & isotherm modelling**

**Hesham H. El-Feky<sup>\*</sup>, Alaa S. Amin and Mostafa Y. Nassar**

*Department of Chemistry, Faculty of Science, Benha University, Benha, Egypt*

*\* Corresponding author: E-mail address: [hesham.elfeky@fsc.bu.edu.eg](mailto:hesham.elfeky@fsc.bu.edu.eg), Phone: +201060204453*

**Abstract:**

The synthesis, characterization and capacity studies of co-polymerized Al<sub>2</sub>O<sub>3</sub> nanocomposites capable of adsorbing with Hg(II) ions are reported. Al<sub>2</sub>O<sub>3</sub> nanoparticles was fabricated with combustion synthesis using inexpensive mixed fuels. Nanocomposite of poly (aniline-CO-O-anthranilic acid) (PANAA/ Al<sub>2</sub>O<sub>3</sub>) was synthesized by chemical oxidative polymerization of anthranilic acid and aniline co-monomers at equimolar ratios (1:1) with the Al<sub>2</sub>O<sub>3</sub> nanostructure. The product was characterized by FT-IR, XRD, SEM and TEM techniques. The adsorption behaviors of the toxic Hg(II) were studied. The equilibrium isotherm, kinetics parameters and the thermodynamics investigations of the adsorption process were calculated. Thermodynamics investigations also confirmed that the adsorption capacity of Hg(II) on each adsorbent was spontaneous and exothermic.

**Keywords:** polymer, nanocomposites, combustion, Mercury and adsorption

## **1. Introduction:**

The world is facing bitter difficulties due to the increase demands for clean water as the available stocks of clean water are decreasing as a result of population growth, development of advanced technologies and increasing demands from a numerous of users. Clean water is free of hazardous waste streams and chemicals, is essential for the life of human. It becomes a critical feed stock in a variety of industries including electronics, pharmaceuticals and food. Clean water can be obtained either through typically ground water or by treating water to improve its chemical, microbiological, physical and radiological characteristics to remove their pollutant load (e.g., fecal bacteria, viruses, heavy metals, organic chemicals and biological oxygen demand) prior to being discharged safely into the environment[1-5] .

The extraction of hazardous chemicals from wastewater and drinking water is one of the most important aims of pollution control. For this reason, different chemical, physical and biological treatment methods have been developed to solve the problem of water pollution[6]. These methods include nanofiltration, adsorption, reverse osmosis, chemical precipitation, anion exchange membrane and oxidation with chlorine, ozone or hydrogen peroxide. Among them, adsorption and photocatalysis play an important role in the field of water treatment. Adsorption is considered a very efficient method as it is a simple method which offers flexibility in design and operation. Most adsorption processes are reversible; therefore, the adsorbents can be regenerated by suitable desorption processes for multiple use by relatively low-cost process and easy to apply[7, 8].

On the other hand, some metals (e.g., As, Hg, Cd and Pb) are highly toxic at very low concentration with no known benefit for human health. They can

accumulate in the body, growing up in fat cells, bones, glands, and hair, and lead to a dizzying array of chronic diseases. Their toxicity can cause reducing in mental and central nervous function, lower energy levels, and damage to lungs, kidneys, vital organs and liver [9, 10]. In this research work, Mercury(II) was selected as examples of heavy metals of concern. Mercury has especially received increasing attention as a serious pollutant due to its toxicity and bio-accumulative properties. Mercury does not metabolize. That is, it does not break down in the body, and as a result it accumulates. When mercury enters the human body, it acts as a neurotoxin, interfering with the brain and nervous system and can also harm the gastrointestinal tract. Symptoms related to mercury poisoning include loss of fluids and electrolytes, edema, lethargy, tremors, hyper-excitability, loosening of the teeth, etc. The concentration of mercury in drinking water is up to 300 mg / dm<sup>3</sup> and in highly industrialized areas it can reach up to 700 mg / dm<sup>3</sup>. 80% of mercury absorbed by the respiratory system is retained in the body. The concentration of mercury vapor over 1 mg / m<sup>3</sup> damages lung tissue and cause sever pneumonia. The classic symptoms of metallic mercury vapor poisoning are manifested by tremor, inflammation of the gums and mental disorders[11-20].

The suitable methods for the remediation of heavy toxic metals[21], consists of adsorption[22, 23], chemical precipitation[24, 25], ion exchange[26, 27], membrane filtration[28-30], coagulation[31, 32] and biosorption processes[33-36]. It is notable that most of these methods have one or more drawbacks in wastewater treatment; however, on the other hand, adsorption method still has the superiority over all methods due to its simplicity, high efficiency, cheapness, and regeneration of the adsorbents[37, 38]. Therefore, various adsorbents have been suggested for treatment of wastewaters from toxic metals. Recently, a considerable attention has been paid to utilizing nanomaterials, including metal oxides, as nano-adsorbents for

decontamination of wastewaters because of their high surface area, large numbers of active sites, and high stability. Among different nano-adsorbents, nano-sized aluminum oxide ( $\text{Al}_2\text{O}_3$ ) has received a significant consideration for decontamination of wastewater attributable to its lower cost, chemical stability, non-toxicity, simple production and large surface area[39-41]. many synthetic methods have been adopted for the preparation of  $\text{Al}_2\text{O}_3$  nanoparticles such as laser vaporization, precipitation, hydrothermal, precipitation, sol-gel, combustion, micro-emulsion, chemical gas phase deposition, and laser vaporization technique[42-46]. However, due to the scalability, feasibility, and low-cost of the combustion process, this synthesis route has aroused the interests of many research groups[47-51]. Moreover, reports on the synthesis of  $\text{Al}_2\text{O}_3$  nanoparticles via a combustion or sol-gel combustion route are still limited. Here, we have reported the combustion synthesis of aluminum oxide nanoparticles using inexpensive fuels such as citric acid, oxalic acid, tartaric acid and urea.

The integration of nanosized materials into functional organic materials or polymers has been a growing field during the last decade. Significant progress in this field has been made by integrating the unique properties of the conductive polymers with those of various nano particles(NPs)[52-55]. Conductive polymer nanocomposites (CPNs) are required for application that includes biosensors[56], fire retardants[57, 58], telecom, electronics[59, 60] and for water treatment[61, 62]. In this work, we focus on the synthesis of poly(aniline co-anthranilic acid)/ $\text{Al}_2\text{O}_3$  nanocomposite (PANAA/  $\text{Al}_2\text{O}_3$ ) using the surface initiated polymerization (SIP) method[63-66]. Various experimental factors influencing the adsorption process along with the isotherm models, kinetics, and thermodynamic investigation have been examined.

## 2. Experimental:

### 2.1. Materials and reagents

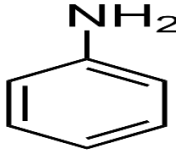
All reagents were of analytical grade and used as received without further purification. Freshly bi-distilled water was used through all experiments. The different chemical reagents used are listed in Table 1. The Structure and characteristics of aniline and anthranilic acid are given in Table [2, 3].

**Table 1. Chemical reagents**

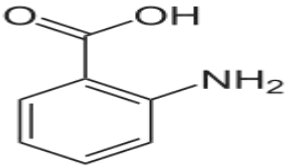
Name	Formula	Purity	Manufacture
Aluminum nitrate	$\text{Al}(\text{NO}_3)_3 \cdot 9\text{H}_2\text{O}$	A.R	Merck
Urea	$\text{NH}_2\text{CONH}_2$	A.R	Fluka
Oxalic acid	$\text{C}_2\text{H}_2\text{O}_4 \cdot 2\text{H}_2\text{O}$	A.R	Sigma-Aldrich
Citric acid	$\text{C}_6\text{H}_8\text{O}_7$	A.R	Sigma-Aldrich
Tartaric acid	$\text{C}_4\text{H}_6\text{O}_6$	A.R	Merck
Aniline	$\text{C}_6\text{H}_5\text{NH}_2$	A.R	Sigma-Aldrich
Anthranilic acid (2-Aminobenzoic acid)	$\text{C}_6\text{H}_4(\text{NH}_2)(\text{CO}_2\text{H})$	A.R	Sigma-Aldrich
Potassium di- chromate	$\text{K}_2\text{Cr}_2\text{O}_7$	A.R	Merck

Mercuric chloride	HgCl <sub>2</sub> .2H <sub>2</sub> O	A.R	Merck
-------------------	--------------------------------------	-----	-------

**Table 2. structure and characteristics of aniline.**

Compound	Aniline
Structure	
Molecular formula	C <sub>6</sub> H <sub>5</sub> NH <sub>2</sub>
IUPAC name	Benzene amine
Density	1.02 g/ml
Boiling point	184.13 °C
Solubility in water	3.6 g/100 ml at 20 °C
Melting point	-6.3 °C
Appearance	Colorless to yellow liquid

**Table 3. structure and characteristics of anthranilic acid.**

Compound	Anthranilic acid
Structure	
Molecular formula	C <sub>6</sub> H <sub>4</sub> (NH <sub>2</sub> ) (CO <sub>2</sub> H)
IUPAC name	2-Aminobenzoic acid
Density	1.412 g/ml
Boiling point	200 °C

<b>Solubility in water</b>	0.572 g/100 mL (25 °C)
<b>Melting point</b>	146:148 °C
<b>Appearance</b>	white or yellow solid

## **2.2. Preparation of Al<sub>2</sub>O<sub>3</sub> nanostructures**

An auto-combustion method was developed to synthesize Al<sub>2</sub>O<sub>3</sub> nanoparticles utilizing six different mixed fuels: (urea + citric acid), (urea + oxalic acid), (urea + tartaric acid), (citric acid + oxalic acid), (citric acid + tartaric acid) and (oxalic acid + tartaric acid). Al<sub>2</sub>O<sub>3</sub> nanoparticles were prepared by using nona-hydrated Aluminum nitrate [Al (NO<sub>3</sub>)<sub>3</sub>.9H<sub>2</sub>O] as the oxidant precursor and the mixed fuels were used as reductant precursors. The produced Al<sub>2</sub>O<sub>3</sub> samples by using the mixed fuels: (urea + citric acid), (urea + oxalic acid), (urea + tartaric acid), (citric acid + oxalic acid), (citric acid + tartaric acid) and (oxalic acid + tartaric acid) are referred to as A, B, C, D, E and F, respectively. The stoichiometric compositions of the redox mixtures for the combustion have been calculated based on the total oxidizing and reducing valencies of the oxidizer and fuel so that the equivalence ratio,  $\phi_c$  is unity (i.e.  $\phi_c = (O/F) = 1$ ), and consequently the energy released by the combustion is maximum for each reaction[67, 68]. In a typical synthesis process:20 ml of Al(NO<sub>3</sub>)<sub>3</sub>.9H<sub>2</sub>O (7.5 g, 0.02 mol) was mixed with an aqueous hot solution (50ml), containing [(1.5g, 0.025 mol urea) + (1.74g, 0.0083mol citric acid)] and the reaction was heated at 80 °C, and allowed to stir for 1h.

The produced solution was gelled while heating at 120 °C. The formed gel was ignited on a hot plate at 350 °C give a dry and grey mass which was calcined in an electric furnace at various temperature like 600 °C and 800°C for 4h giving sample A<sub>600</sub> and A<sub>800</sub>, respectively. The produced Aluminum oxide samples using different mixed fuels (B, C, D, E and F) were prepared by applying similar conditions. Hence,

likewise, the subscripts 600 and 800 (for B<sub>600</sub>, B<sub>800</sub>, C<sub>600</sub>, C<sub>800</sub>, D<sub>600</sub>, D<sub>800</sub>, E<sub>600</sub>, E<sub>800</sub>, F<sub>600</sub> and F<sub>800</sub>) are referred to the calcination temperature; 600 and 800 °C.

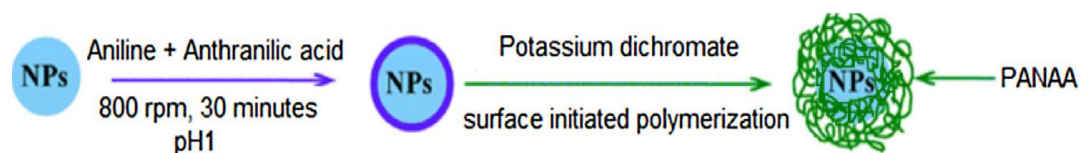
### **2.3. Preparation and characterization of PANAA [poly (aniline-CO-O-anthranilic acid)]:**

The synthesis of PANAA was done by chemical oxidative polymerization of anthranilic acid and aniline co-monomers at equimolar ratios (1:1). 8 ml conc. HCl was added to 0.93 g aniline. 1.37 g anthranilic acid was added to the mixture under magnetic stirring with 800 rpm at room temperature. 30 ml distilled water was added to the previous solution of co-monomers. Potassium dichromate (initiator, 60 ml, 1M) was added slowly drop by drop into the co-monomers mixture for 30 min<sub>s</sub>. Then the formed mixture was left for three hours. PANAA was precipitated on the surface of nano particles. Finally, the precipitate was filtered using a Buchner funnel and washed several times with distilled water and ethanol to remove monomers, oligomers and excess oxidant until the filtrate become almost colorless. At 80° C the precipitate was dried for 24h[63-66].

### **2.4. Preparation and characterization of PANAA/Al<sub>2</sub>O<sub>3</sub> nanocomposite:**

Al<sub>2</sub>O<sub>3</sub> nanoparticles were coated with different loadings of poly (aniline co-anthranilic acid “PANAA”) copolymer by using surface-initiated polymerization (SIP) method[63-66]. 8 ml conc. HCl was added to 0.93 g aniline. 1.37 g anthranilic acid was added to the mixture under magnetic stirring with 800 rpm at room temperature. 30 ml distilled water was added to the previous solution of co-monomers then mixed with 0.5 g of E<sub>800</sub> dispersed in 50 ml distilled water. 60 ml of 1 M K<sub>2</sub>Cr<sub>2</sub>O<sub>7</sub> was added slowly drop by drop to the PANAA/Al<sub>2</sub>O<sub>3</sub> mixture for 1h at room temperature. The formed PANAA/Al<sub>2</sub>O<sub>3</sub> composite was collected by

filtration using a Buchner funnel and washed several times with distilled water and ethanol to remove monomers, oligomers and excess oxidant until the filtrate become almost colorless. At 80° C the precipitate was dried for 24h.



**Scheme 1. Preparation of nanosized oxide-polymer**

### **2.5. Adsorption experiment:**

The adsorption capacity of E<sub>800</sub> and (PANAA/E<sub>800</sub>) nanocomposites were measured in a batch method performed under a continuous magnetic stirring using a solution of Hg(II) as an adsorbate model. Different factors affecting the adsorption process such as metal solution pH (2.6-9.4), contact time (1-24hr), temperature (25-50° C), initial concentration of metal solution (10-70 ppm) and the effect of dose (0.025-0.1 g). according to batch method, 50 ml of an aqueous metal solution of a desired concentration was prepared by diluting a stock solution and the pH was adjusted using 0.1M HCl or 0.1M NaOH solutions.

Afterwards, a known mass of the nanoparticle sample was added producing a suspension in the conical flask then allowed to stir magnetically (400rpm) for a definite time at room temperature. The temperature, concentration and the dose of adsorbent were studied. After a definite time of stirring, an aliquot was taken out of the flask and by centrifuging at 5000 rpm for 5 min the adsorbent was separated. The concentration of the remaining metal concentration in the supernatant solution was determined by using a Perkin Elmer flame atomic absorption spectrophotometer, model 2380. The obtained data were used to calculate the adsorption capacities ( $q_t$ , mg g<sup>-1</sup>) and the metal removal efficiencies (%removal) using equation (1) and (2).

$$q_t = [V (C_0 - C_t)] / m \quad (1)$$

$$\% \text{removal} = [(C_0 - C_t) / C_0] \times 100 \quad (2)$$

Where  $C_0$  and  $C_t$  are the metal concentrations in  $\text{mg L}^{-1}$  at time = 0 and  $t$  respectively in solution,  $V$  is the volume of dye solution (L), and  $m$  is the mass of dry adsorbent (g). Additionally, by utilizing Eq. (3), the equilibrium adsorption capacities of the adsorbents,  $q_e$  (mg/g), can be determined.

$$Q_e = [V (C_0 - C_e)] / m \quad (3)$$

where,  $C_e$  (mg/L) is the dye concentration at equilibrium in the supernatant after separation of the adsorbent; and  $V$ ,  $m$ , as well as  $C_0$  have the aforementioned meaning.

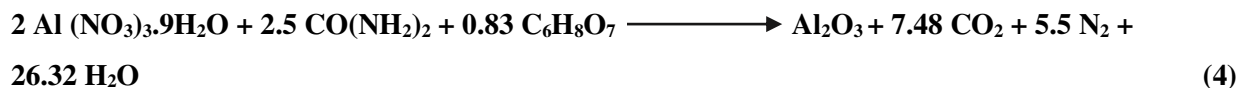
### **3. Results and discussion**

#### **3.1. Synthesis and characterization of $\text{Al}_2\text{O}_3$ nanostructures**

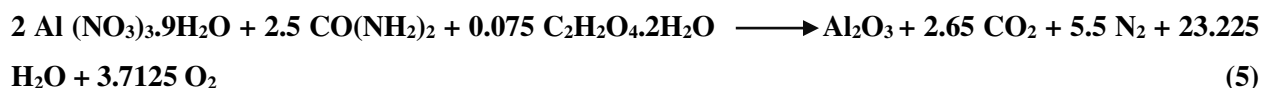
An auto-combustion method was developed to synthesize  $\text{Al}_2\text{O}_3$  nanoparticles utilizing six different mixed fuels: (urea + citric acid), (urea + oxalic acid), (urea + tartaric acid), (citric acid + oxalic acid), (citric acid + tartaric acid) and (oxalic acid + tartaric acid).  $\text{Al}_2\text{O}_3$  nanoparticles were prepared by using nona-hydrated Aluminum nitrate [ $\text{Al}(\text{NO}_3)_3 \cdot 9\text{H}_2\text{O}$ ] as the oxidant precursor and the mixed fuels were used as reductant precursors. The produced  $\text{Al}_2\text{O}_3$  samples by using the mixed fuels: (urea + citric acid), (urea + oxalic acid), (urea + tartaric acid), (citric acid + oxalic acid), (citric acid + tartaric acid) and (oxalic acid + tartaric acid) are referred to as A, B, C, D, E and F, respectively. The stoichiometric compositions of the redox mixtures for the combustion have been calculated based on the total oxidizing [5] and reducing [5] valencies of the oxidizer and fuel so that the equivalence ratio,  $\phi_c$  is unity (i.e.  $\phi_c = (\text{O}/\text{F}) = 1$ ), and consequently the energy released by the combustion

is maximum for each reaction. The proposed combustion reactions of aluminum nitrate and the fuels of interest can be presented by equations 4–9 (Scheme 1).

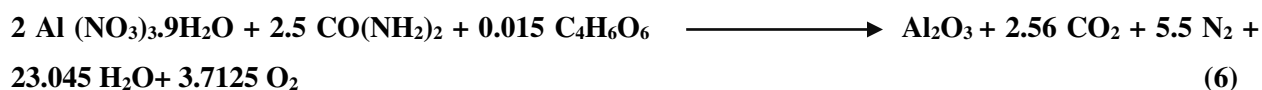
**(a) (urea + citric acid)**



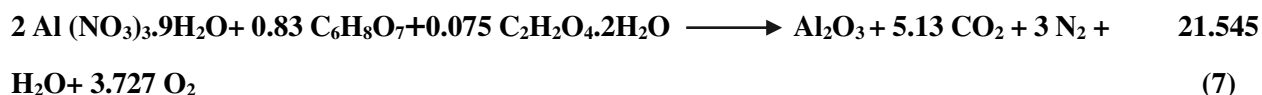
**(b) (urea + oxalic acid)**



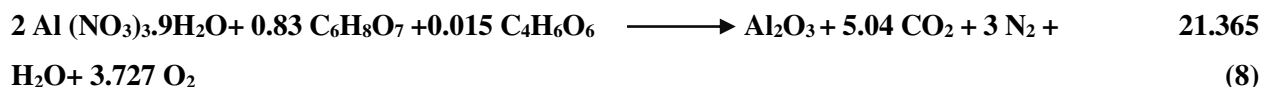
**(C) (urea + tartaric acid)**



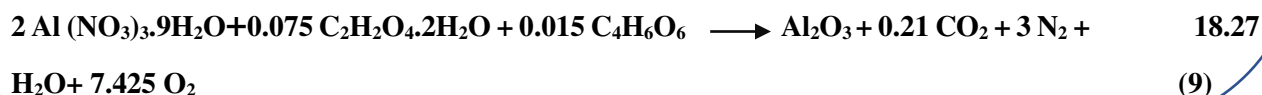
**(d) (citric acid + oxalic acid)**



**(e) (citric acid + tartaric acid)**



**(f) (oxalic acid + tartaric acid)**



**Scheme 1.** The proposed combustion reactions of aluminum nitrate with the different mixed fuels

3.1.1. XRD analysis of prepared Al<sub>2</sub>O<sub>3</sub>

The phase purity and the crystal structure of the prepared nanoparticles were identified by measuring the XRD pattern analysis. XRD patterns of the Aluminum oxide nanoparticles produced by the combustion of the dried gel at 600 and 800 °C are shown in Figs. 14 and 15, respectively. It is obvious that the product formed by

600 °C was almost amorphous not a crystalline product (Fig. 1). consequently, it was necessary to increase the calcination temperature to 800 °C for all samples to obtain crystallite forms from the aluminum oxide using the different mixed fuels.

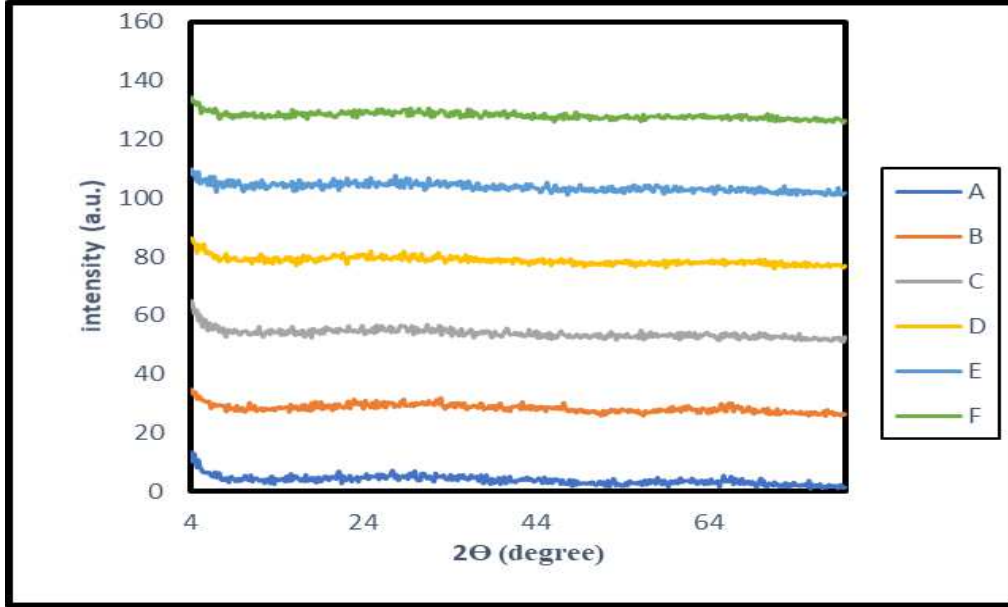


**Fig. 1.** XRD patterns of Al<sub>2</sub>O<sub>3</sub> samples (A, B, C, D, E and F) calcined at 600 °C.

In case of the products (A, B, C, D and F) except (E) formed by 800 °C, the sites and intensity of the diffraction peaks are consistent with the standard pattern for JCPDS card No. (00-010-0425) Aluminum oxide Fig. 2. XRD patterns of Al<sub>2</sub>O<sub>3</sub> samples (A, B, C, D and F) except (E) calcined at 800 °C for 4h are almost identical showing broad peaks, indicating small crystalline size of the particles and the fine nature. The average particle size [D] for all samples was obtained according to the Debye-Scherrer formula using the following equation[69].

$$D = 0.9\lambda / \beta \cos\Theta \quad (10)$$

Where  $\beta$  is the full-width at half-maximum (FWHM) value of XRD diffraction lines, the wavelength  $\lambda = 0.154056$  nm and  $\Theta$  is the half diffraction angle of  $2\Theta$ . The lattice constants are equal ( $a = b = c = 7.9 \text{ \AA}$ ) ensure the formation of a cubic structure. The diffraction peaks at  $19.451^\circ$ ,  $37.604^\circ$ ,  $39.492^\circ$ ,  $45.863^\circ$ ,  $60.899^\circ$  and

67.034° are indexed to the following planes (1 1 1), (3 1 1), (2 2 2), (4 0 0), (5 1 1) and (4 4 0) of the cubic unit cell. The average particle size was found to be 4.98, 5.5, 6.74, 4.82 and 5.66 for samples A, B, C, D and F calcined at 800 °C, respectively.

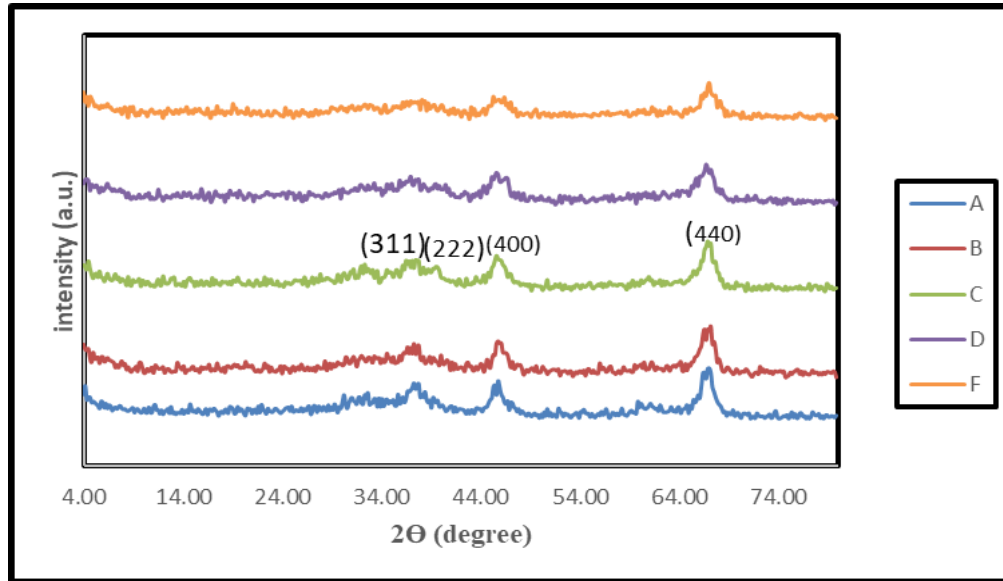


**Fig. 2.** XRD patterns of Al<sub>2</sub>O<sub>3</sub> samples (A, B, C, D and F) calcined at 800 °C

For sample (E) formed by 800 °C, the sites and intensity of the diffraction peaks are consistent with the standard pattern for JCPDS card No. (00-042-1468) Aluminum oxide Fig. 3. The lattice constants are equal ( $a = b = 4.7588$  and  $c = 12.9920$  Å) ensure the formation of a Rhombohedral structure. The diffraction peaks at 25.577°, 35.151°, 37.785°, 43.363°, 52.559°, 61.305°, 66.522°, 68.209°, and 76.882° are indexed to the following planes (0 1 2), (1 0 4), (1 1 0), (1 1 3), (0 2 4), (0 1 8), (2 1 4), (3 0 0) and (1 0 10) of the unit cell. The average particle size was found to be 4.68.

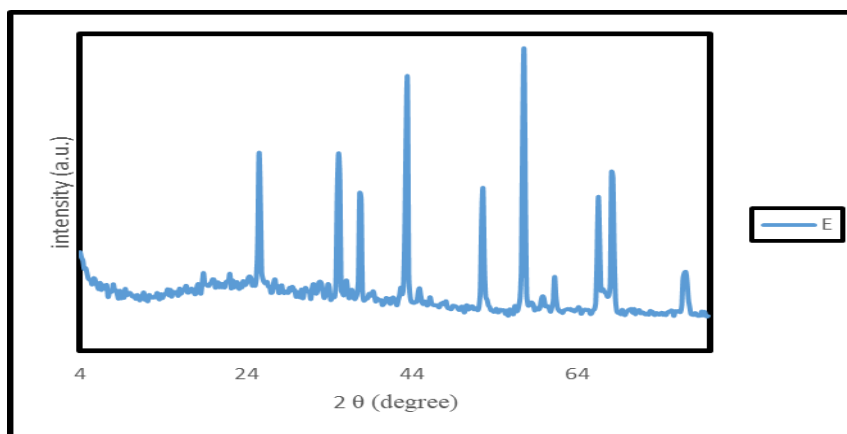


**Fig. 3.** XRD patterns of Al<sub>2</sub>O<sub>3</sub> (E) calcined at 800 °C

### **3.1.2. FT-IR study of Al<sub>2</sub>O<sub>3</sub> nanoparticles**

The infrared spectra of the as-prepared Al<sub>2</sub>O<sub>3</sub> nano-powders (A, B, C, D, E and F) before calcination and calcined at 800 °C for 4h are shown in Fig. 4 and Fig. 5, respectively, and it seems that the six spectra are almost identical. In Fig. 4, the wide absorption band at 3318 cm<sup>-1</sup> represents the –OH stretching vibration and reveals the presence of hydroxyl groups. The band at 1620 cm<sup>-1</sup> is OH bending vibration. The absorption bands in the IR spectra, the bands from 1405 to 1628.84 cm<sup>-1</sup> indicate the formation of alumina. The peak around 1071.79 cm<sup>-1</sup> is attributed to Al–O–C bond between the Al<sup>3+</sup> and the used fuel. In Fig.5, the Al<sub>2</sub>O<sub>3</sub> samples exhibited characteristic frequency in the region of 400–700 cm<sup>-1</sup> correspond to the existence of Al<sub>2</sub>O<sub>3</sub>[70]. The peak which is attributed to Al–O–C bond between the Al<sup>3+</sup> and the used fuel disappeared in Fig. 18 reveals complete removal of residual organic group from the powder calcined at 800 °C. the calcination caused the Al-OH groups and the deformation and O-H stretching vibration of weakly-bound water in the sample to disappear.

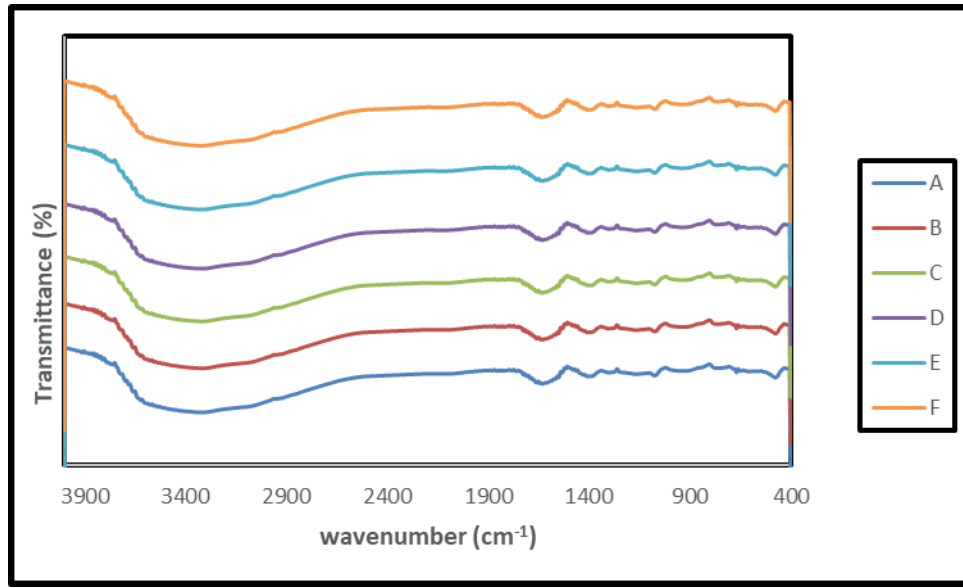


**Fig. 4.** FT-IR spectra of Al<sub>2</sub>O<sub>3</sub> samples (A, B, C, D, E and F) before calcination

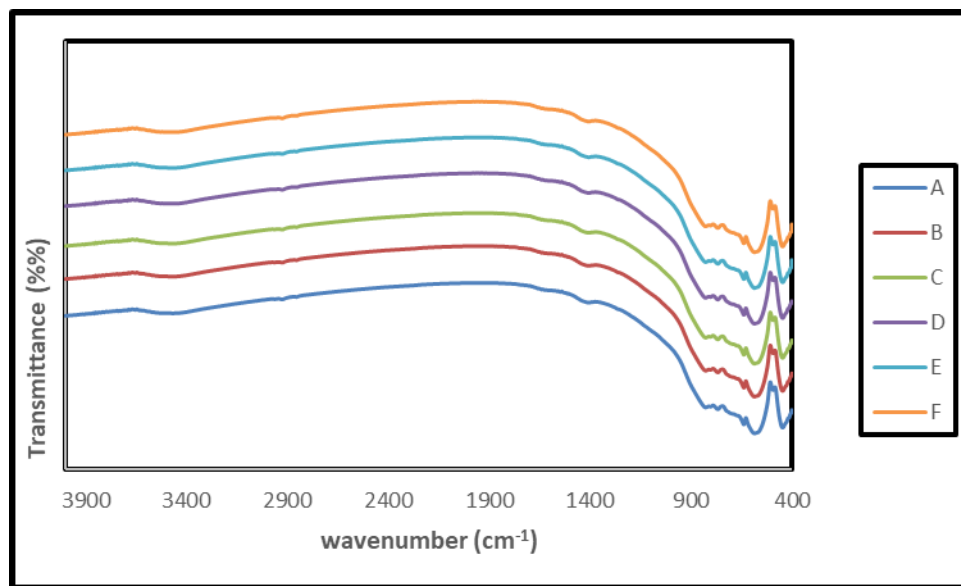
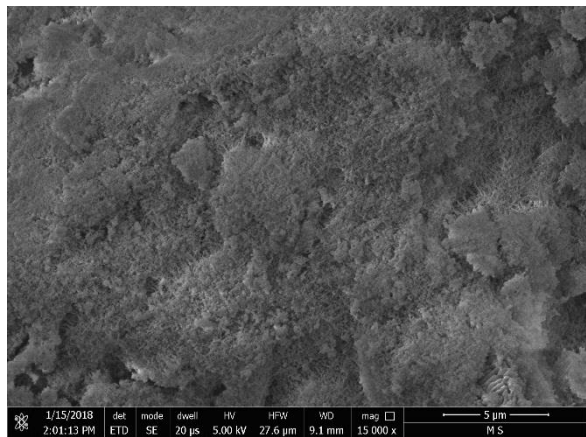
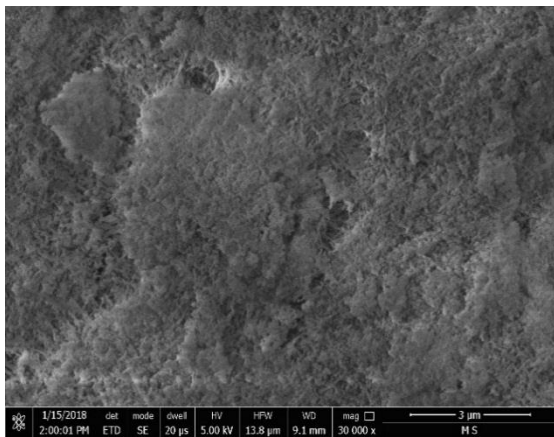


**Fig. 5.** FT-IR spectr of Al<sub>2</sub>O<sub>3</sub> samples (A, B, C, D, E and F) calcined at 800 °C

### 3.1.3. Morphology investigation of Al<sub>2</sub>O<sub>3</sub> nanoparticles

#### 3.1.3.1 Field emission scanning electron microscopy (FE-SEM) of Al<sub>2</sub>O<sub>3</sub> nanoparticles

Morphologies of the as-prepared  $\text{Al}_2\text{O}_3$  sample calcined at  $800\text{ }^\circ\text{C}$  ( $\text{E}_{800}$ ) was investigated by using field emission scanning electron microscopy (FE-SEM) and presented in Fig. 6. From SEM micrographs of  $\text{E}_{800}$  powders, rough surfaces and many visible mesopores are observable in the micrographs with a wide distribution. The reaction takes place with no flame which results in amorphous product and agglomerated particles in nano and micro scales. The average size of these shapes is about  $1.8\text{ }\mu\text{m}$ . In order to achieve the reliable result, the secondary particle size should be evaluated by TEM images with higher magnification.



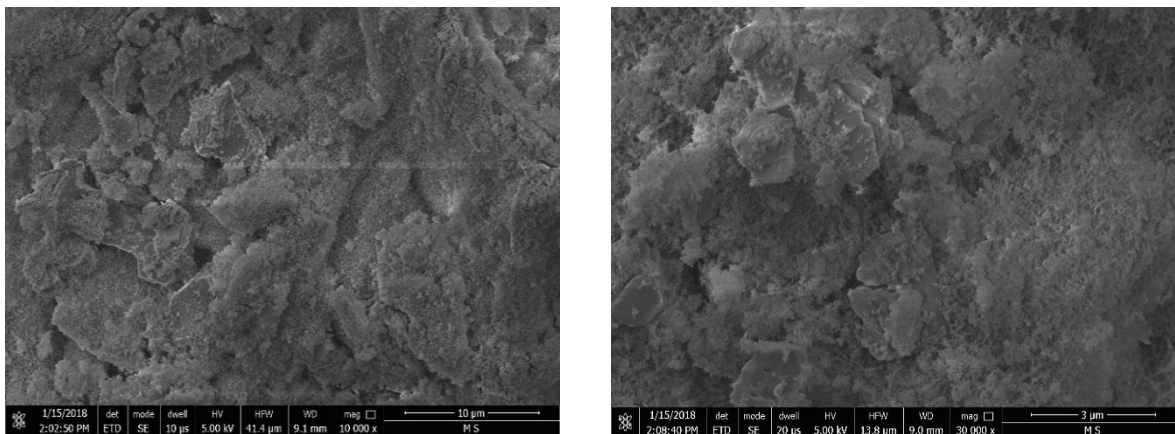


**Fig. 6. FE-SEM images of Al<sub>2</sub>O<sub>3</sub> product E calcined at 800 °C**

### **3.1.3.2. High-resolution transmission electron microscopy (HR-TEM) of Al<sub>2</sub>O<sub>3</sub> nanoparticles**

In order to achieve the reliable result, the secondary particle size should be evaluated by high resolution transmission electron microscopy (HR-TEM) images with higher magnification. TEM technique has been applied to examine the microstructure of the Al<sub>2</sub>O<sub>3</sub> (E<sub>800</sub>) Fig. 7. As shown in Fig. 7 the product E<sub>800</sub> is composed of dispersed hexagonal and cubic particles with an average diameter of 11 nm which is compatible with the crystalline size calculated from the XRD studies.

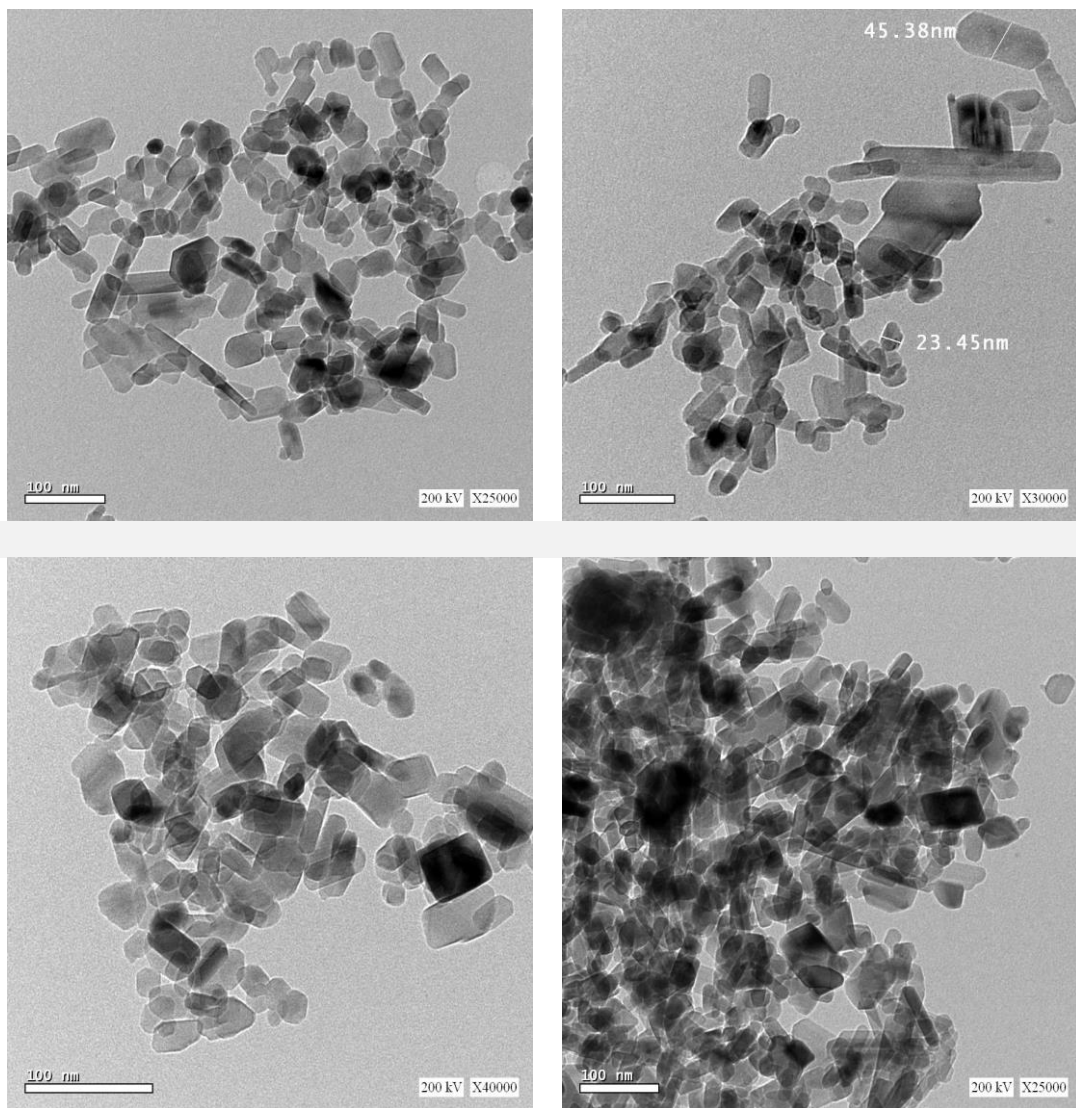


**Fig. 7.** HR-TEM images of Al<sub>2</sub>O<sub>3</sub> product (E) calcined at 800 °C

### **3.2. Preparation and characterization of PANAA [poly (aniline-CO-O-anthranilic acid)]**

#### **3.2.1. Preparation of of PANAA [poly (aniline-CO-O-anthranilic acid)]**

The synthesis of PANAA was done by chemical oxidative polymerization of anthranilic acid and aniline co-monomers at equimolar ratios (1:1). 8 ml conc. HCl was added to 0.93 g aniline. 1.37 g anthranilic acid was added to the mixture under

magnetic stirring with 800 rpm at room temperature. 30 ml distilled water was added to the previous solution of co-monomers. Potassium dichromate (initiator, 60 ml, 1M) was added slowly drop by drop into the co-monomer's mixture for 30 min<sub>s</sub>. Then the formed mixture was left for three hours. PANAA was precipitated on the surface of nano particles. Finally, the precipitate was filtered using a Buchner funnel and washed several times with distilled water and ethanol to remove monomers, oligomers and excess oxidant until the filtrate become almost colorless. At 80° C the precipitate was dried for 24h.

### **3.2.2. Characterization of PANAA [poly (aniline-CO-O-anthranilic acid)].**

#### **3.2.2.1. X-ray Diffraction analysis (XRD) of PANAA [poly (aniline-CO-O-anthranilic acid)]**

The x-ray diffraction patterns of PANAA is shown in Fig. 8. What can be noticed is that there is no crystallinity for PANAA.

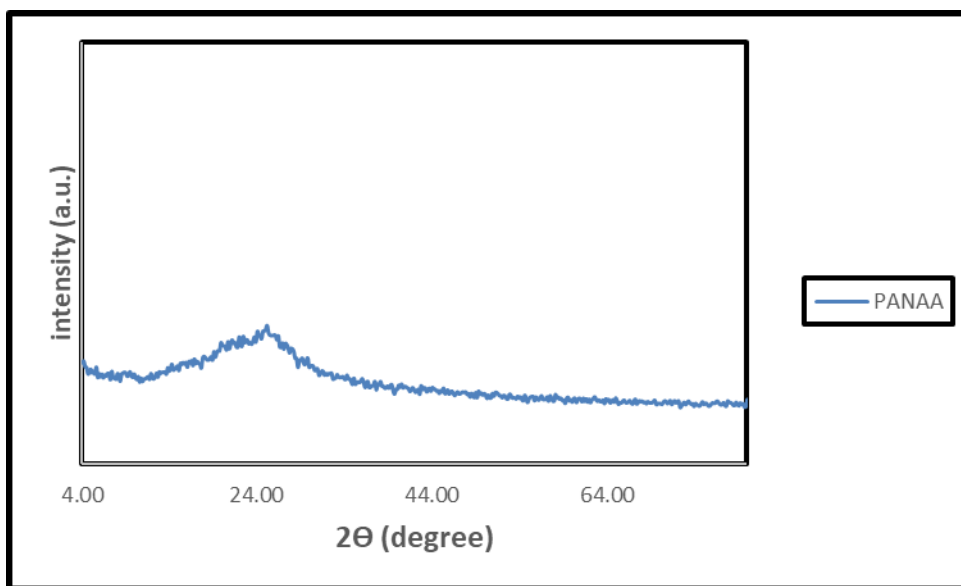


**Fig. 8.** XRD patterns of PANAA

### 3.2.2.2. FT-IR study of PANAA

The structure of PANAA copolymer was confirmed by using FT-IR spectroscopy Fig. 9: the band at  $1586.66\text{ cm}^{-1}$  and  $1493.75$  were due to the  $\text{C} = \text{C}$  vibrations of quinoid and benzenoid ring stretching of the aromatic ring through the copolymer backbone[71-73]; the band at  $1296.45$ - $1495\text{ cm}^{-1}$  was due to the  $\text{C}-\text{N}$  stretching vibrations of the secondary aromatic amine (quinoid and benzenoid sequence); The strong band at  $1150\text{ cm}^{-1}$  is a characteristic for emeraldine salt (doped with chloride ion). The bands at  $1140\text{ cm}^{-1}$  and  $829\text{ cm}^{-1}$  were due to the  $\text{CH}$  out-of-plane and the stretching in the BBB unit, respectively. The spectra of copolymer showed similar bands as those reported for poly aniline in absence of Anthranilic acid with exception of  $\text{C} = \text{O}$  absorption band at about  $1670$ - $1676\text{ cm}^{-1}$ . Therefore, the copolymer can be distinguished from the homopolymer by this characteristic band. It can be inferred that the *o*-anthranilic acid has been introduced into the polymer chains[74-76]. The carboxylic group in PANAA could be confirmed via the absorption bands of stretching vibration of  $\text{C} = \text{C}$ ,  $(\text{C}-\text{C})$ ,  $\text{COOH}$  groups at about  $1722.19\text{ cm}^{-1}$ .

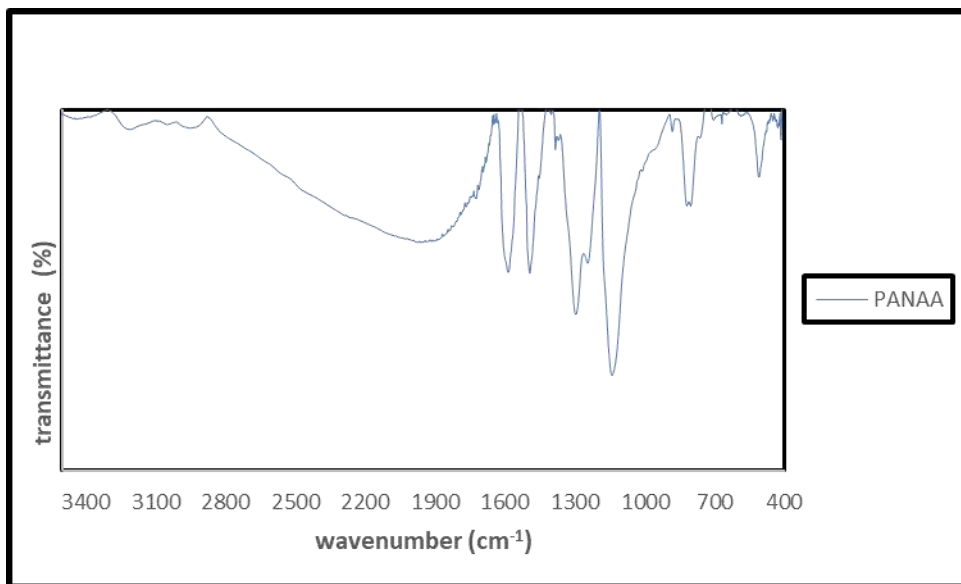


**Fig. 9.** FT-IR spectra of PANAA

### **3.3. Preparation and characterization of PANAA/Al<sub>2</sub>O<sub>3</sub> nanocomposite**

#### **3.3.1. Preparation of PANAA/Al<sub>2</sub>O<sub>3</sub> nanocomposite**

Al<sub>2</sub>O<sub>3</sub> nanoparticles were coated with different loadings of poly (aniline co-anthranilic acid “PANAA”) copolymer by using surface-initiated polymerization (SIP) method. 8 ml conc. HCl was added to 0.93 g aniline. 1.37 g anthranilic acid was added to the mixture under magnetic stirring with 800 rpm at room temperature. 30 ml distilled water was added to the previous solution of co-monomers then mixed with 0.5 g of E<sub>800</sub> dispersed in 50 ml distilled water. 60 ml of 1 M K<sub>2</sub>Cr<sub>2</sub>O<sub>7</sub> was added slowly drop by drop to the PANAA/Al<sub>2</sub>O<sub>3</sub> mixture for 1h at room temperature. The formed PANAA/Al<sub>2</sub>O<sub>3</sub> composite was collected by filtration using a Buchner funnel and washed several times with distilled water and ethanol to remove monomers, oligomers and excess oxidant until the filtrate become almost colorless. At 80° C the precipitate was dried for 24h.

#### **3.3.2. Characterization of PANAA/Al<sub>2</sub>O<sub>3</sub> nanocomposite**

##### **3.3.2.1. X-ray Diffraction analysis (XRD) of PANAA/Al<sub>2</sub>O<sub>3</sub> nanocomposite**

The x-ray diffraction patterns of PANAA, E<sub>800</sub> and PANAA / E<sub>800</sub> nanocomposites are shown in Fig. 10. What can be noticed is that there is no crystallinity for PANAA. There was no change in PANAA/E<sub>800</sub> compared to standard pattern for JCPDS card No. (00-042-1468) Aluminum oxide. Consequently, there is no chemical bonding between E<sub>800</sub> and PANAA in the prepared nanocomposites. The interaction between them is physically based.

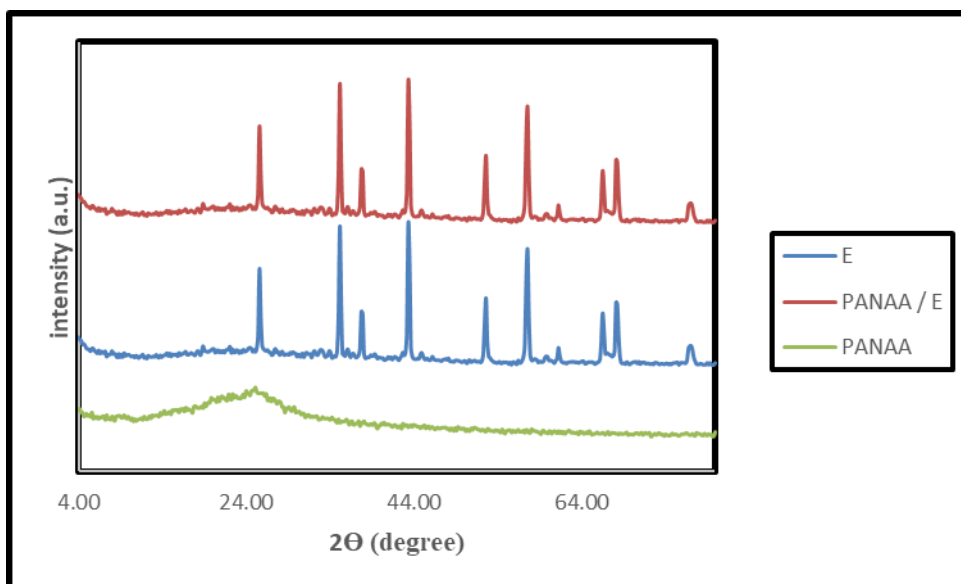


**Fig. 10.** XRD patterns of E<sub>800</sub>, PANAA and PANAA/E<sub>800</sub> nanocomposites.

### 3.3.2.2. FT-IR study of PANAA/Al<sub>2</sub>O<sub>3</sub> nanocomposite

The FT-IR spectra of the neat PANAA, E<sub>800</sub> and PANAA / E<sub>800</sub> nanocomposites are shown in Fig. 11. The vibration bands at 1586.66 cm<sup>-1</sup> and 1493.75 were due to the C = C vibrations of quinoid and benzenoid ring stretching of the aromatic ring for PANAA were shifted to 1584.03 cm<sup>-1</sup> and 1495.32 cm<sup>-1</sup>, respectively for PANAA / E.

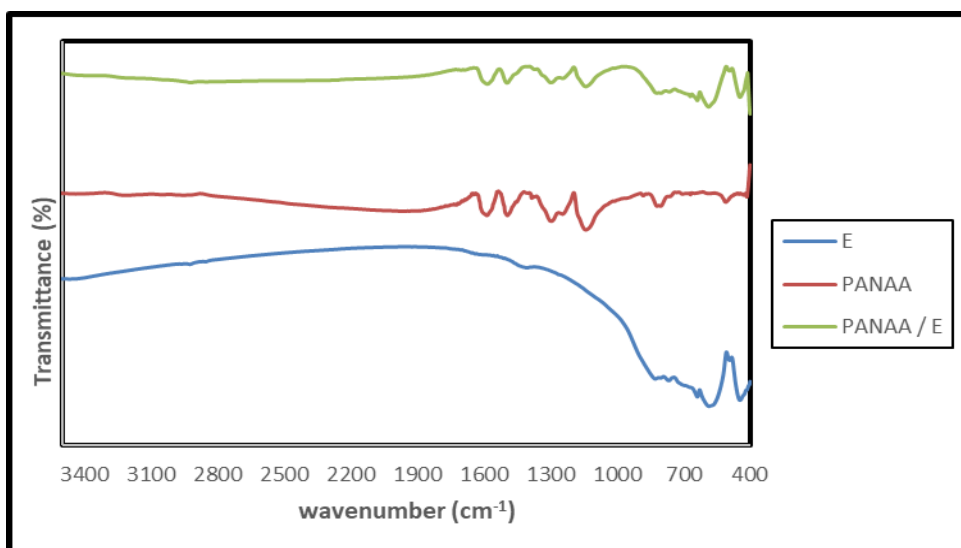


**Fig. 11.** FT-IR spectra of E<sub>800</sub>, PANAA and PANAA/E<sub>800</sub> nanocomposites.

### 3.3.3. Morphology study of [PANAA/ Al<sub>2</sub>O<sub>3</sub>] composite

#### 3.3.3.1. Field emission scanning electron microscopy (FE-SEM) of [PANAA / Al<sub>2</sub>O<sub>3</sub>] composite

The surface morphology and particle size of PANAA/ Al<sub>2</sub>O<sub>3</sub> nanocomposite were investigated Fig. 12. The SEM images show that the size of the PANAA/ Al<sub>2</sub>O<sub>3</sub> nanocomposites finely dispersed nanoscale. The regular shape of the PANAA/ Al<sub>2</sub>O<sub>3</sub> nanocomposites can be the result of PANAA presence as it minimizes the aggregation of Aluminum oxide particles.

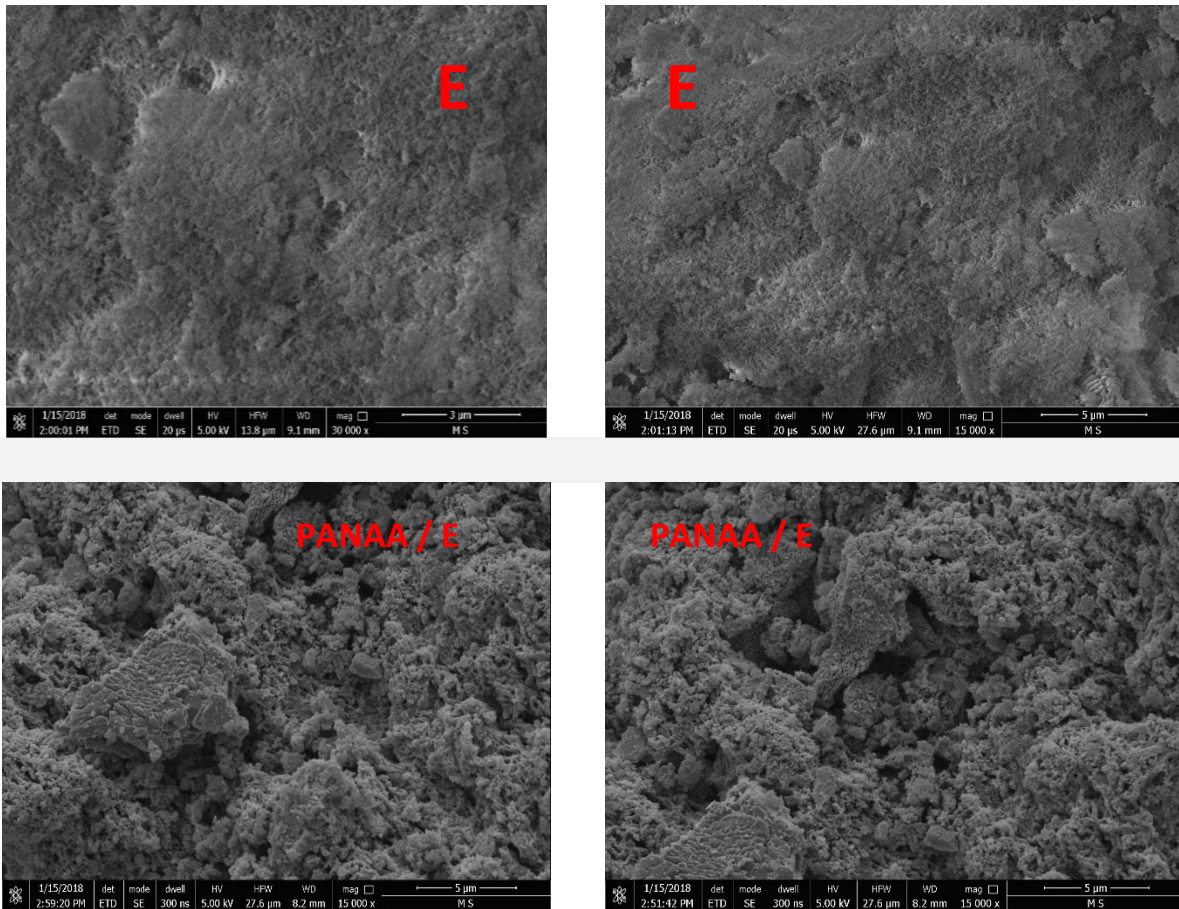


Fig. 12. FE-SEM images of Al<sub>2</sub>O<sub>3</sub> and PANAA / E products

### **3.3.3.2. Field emission scanning electron microscopy (FE-TEM) of [PANAA / Al<sub>2</sub>O<sub>3</sub>] composite**

The transmission electron microscopy (TEM) images of the PANAA / Al<sub>2</sub>O<sub>3</sub> nanocomposite are shown at different magnifications in Fig. 13. TEM images illustrate particle properties such as shape, size and distribution of nanocomposites. The TEM images of PANAA / Al<sub>2</sub>O<sub>3</sub> nanocomposite shows a dense morphological structure that confirm the coating of PANAA on the surface of Al<sub>2</sub>O<sub>3</sub> particles. we found that the nanocomposites have average diameter of 20 nm.

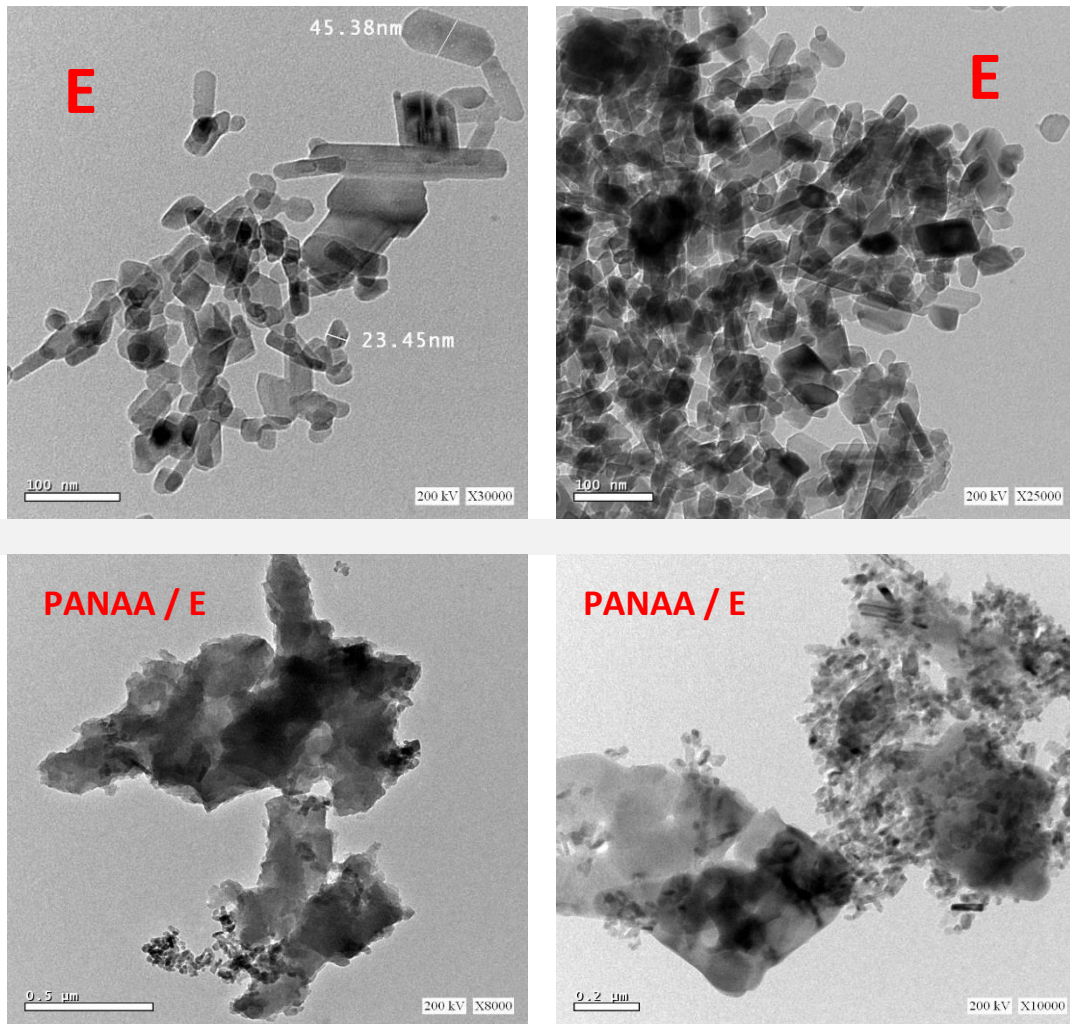


Fig. 13. HR-TEM images of Al<sub>2</sub>O<sub>3</sub> (E) and PANAA / Al<sub>2</sub>O<sub>3</sub>.

### 3.4. Adsorption studies

#### 3.4.1. Characteristic adsorption capacity of prepared samples

Adsorption is an efficient and economically feasible process for the wastewater containing chemically stable pollutants such as heavy metals. We investigated the adsorption properties of the different prepared adsorbents by Hg(II) ions as a toxic pollutant. Adsorption capacity represents one of the more characteristics features to decide which sample is more convenient for heavy metal removal processing. The FT-IR spectra can be used as an evidence for the adsorption process of heavy metals[49, 77]. Fig. 14(a,b) depicts the FT-IR spectra of the prepared adsorbents before and after adsorption of Hg(II). From Fig. 14(a,b), it is observed that the spectrum of Hg(II) metal-loaded for each adsorbent differs from that adsorbent before the adsorption. A new peak appeared approximately at (1373-1385,  $\text{cm}^{-1}$ ) in all spectrum is probably due to the adsorbed Hg(II) ions onto the adsorbent.

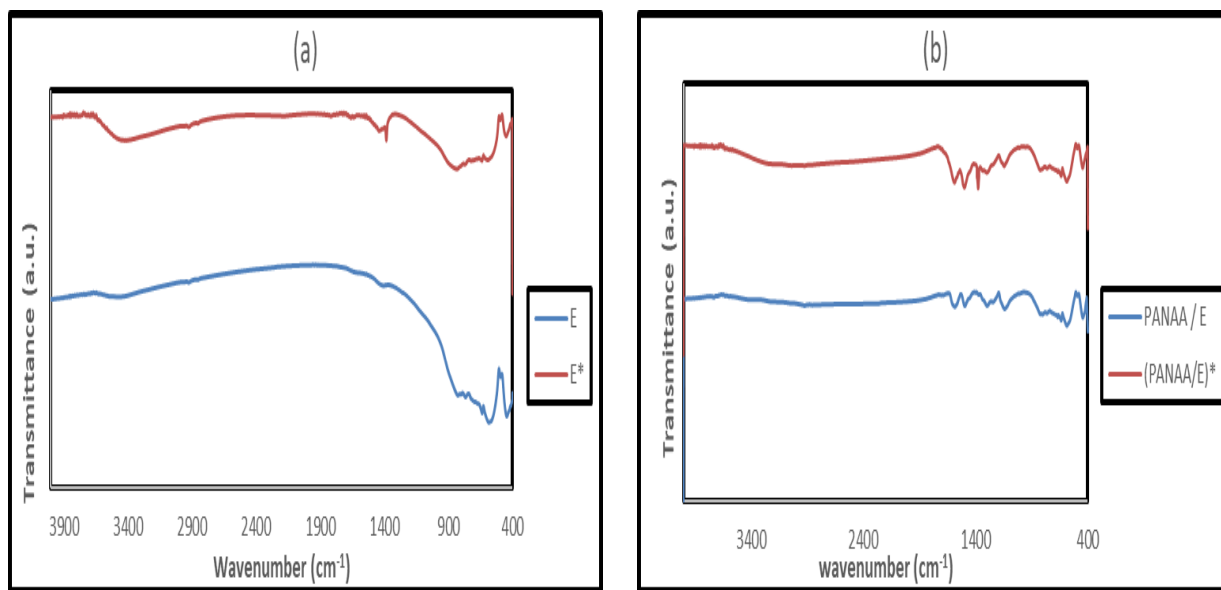


Fig. 14(a,b). The FT-IR spectra before and after adsorption (\*) for a) E, b) PANAA/E

Many factors affecting the Hg (II) expulsion from water such as pH, dosage level of nanoparticles, temperature, contact time and the initial concentration of heavy metal were studied.

### **3.4.2. Factors affect the adsorption process**

#### **3.4.2.1. Effect of pH**

The adsorption progress by protonation and deprotonation of adsorbent surface functional groups are influenced by the pH of the sample. The pH of the solution controls the adsorption behavior of Hg(II) ions onto the adsorbent particles. It affects the solubility of the metal ions in the solution, replaces some of the positive ions found in the active sites and affects the degree of ionization of the adsorbate during the reaction[78]. The effect of initial pH on the sorption of Hg(II) ions onto utilized nano particles was evaluated within the pH range of 2.6-9.53. The metal removal from solution at pH beyond 10 would not give accurate results because precipitation of the ions as hydroxides took place, that was the reason the removal curve became high as there were not mercury ions to be removed (the solution seems to be clear because of the metal precipitation)[79]. The effect of different pH values ranged from 2.6 to 9.53 on the adsorption of Hg(II) by Al<sub>2</sub>O<sub>3</sub> (E<sub>800</sub>) and PANAA / (E<sub>800</sub>) nanocomposites (1 g/L) for 24h contact time was investigated Fig. 15. The initial concentration of Hg(II), adsorbent dose, volume of Hg(II) ions and the stirring rate were set at 20 ppm, 0.05 g, 50 ml and 400 rpm, respectively at 298 K for 24h.

The effect of pH on the adsorption behavior of nano alumina for Hg(II) was shown in Fig. 15. The initial pH of the solution significantly affected the adsorption capacity of the adsorbent; adsorption capacity was highest when pH was 9.43 giving 53 % removal and decreased by lowering pH under the present range of the experimental condition. At lower values, the metal ion uptake was limited in this acidic medium, this can be attributed to the presence of H<sup>+</sup> ions which compete with

the Hg(II) ions for the adsorption sites. Contrarily, the metal ion was about to form metal hydroxide deposition through hydrolysis at higher values of pH[80]. Similarly, the best pH given highest Hg(II) removal was at pH= 9.53 for PANAA / (E<sub>800</sub>) nanocomposite, respectively.

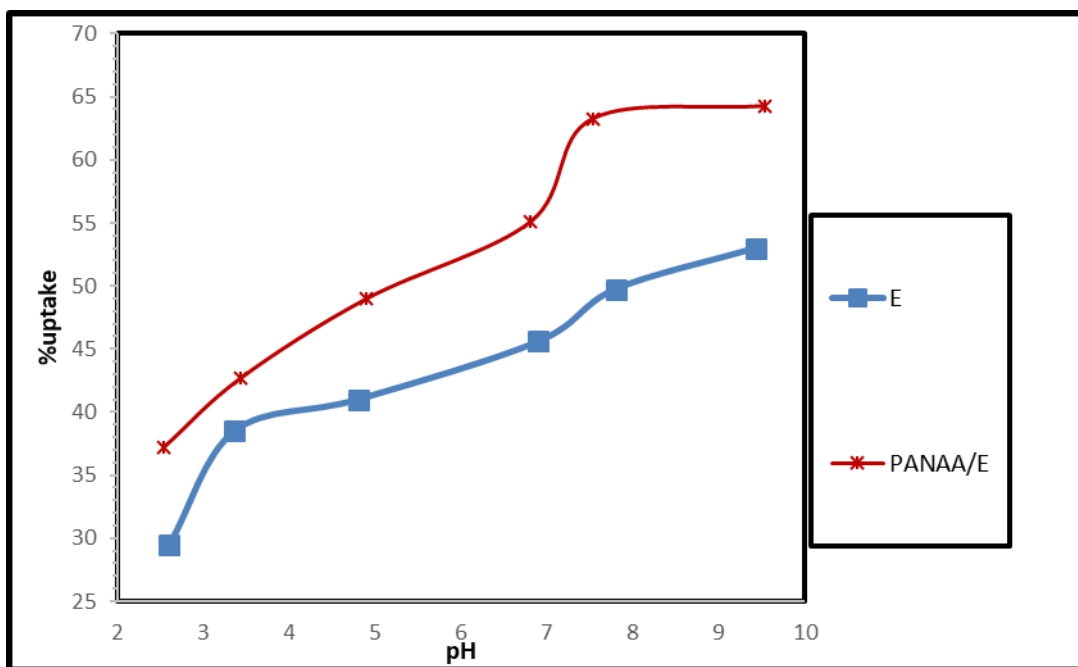


**Fig. 15.** Effect of pH on Hg(II) removal percent using different nano-sized adsorbents.

### 3.4.2.2. Effect of contact time

The contact time between adsorbate and adsorbent is one of the most important parameters that affects the performance of adsorption processes. Thus, the effect of contact time on the performance of Al<sub>2</sub>O<sub>3</sub> (E<sub>800</sub>) and PANAA / (E<sub>800</sub>) nanocomposites in adsorbing Hg(II) was investigated at pH= 9.43 and 9.53, respectively. The dose of adsorbent was 0.05g using different concentration of Hg(II) [10-70] mg/L at 298 K. The adsorption capacities (q<sub>t</sub>, mg/g) of Al<sub>2</sub>O<sub>3</sub> (E<sub>800</sub>) and PANAA / (E<sub>800</sub>) nanocomposites for the adsorption of different conc. of Hg(II) versus the contact time (t, h) were displayed in Fig. 16(a,b) For all adsorbents,

respectively. It could be observed that the adsorption was fast in the initial stages; afterward, it increased slowly with increasing the contact time until it reached the equilibrium state (i.e. the plateau behavior). The change in the rate of Hg(II) adsorption at the initial and later stages is probably due to the presence of large number of active adsorption sites available for adsorption in the beginning of the adsorption process. Then, this number decreased with increasing the contact time by an occupation of the adsorption active sites during the adsorption process. Besides, the slower adsorption rates at longer contact times can be assigned to the slower pore diffusion rate of Hg(II) ions into the nanoparticles. From Fig. 16(a,b), the optimum contact time for Al<sub>2</sub>O<sub>3</sub> (E<sub>800</sub>) and PANAA / (E<sub>800</sub>) nanocomposites for the adsorption of different conc. Hg(II) were at 5h and 4h, respectively.

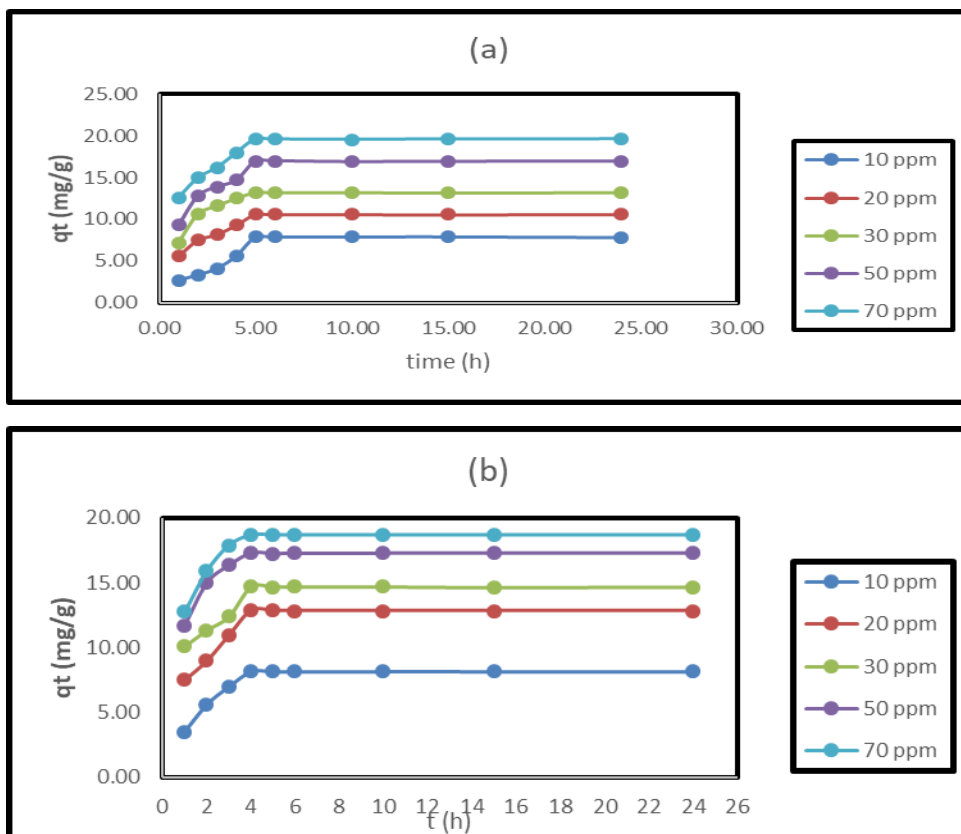


**Fig. 16(a,b).** Effect of contact time on Hg(II) removal percent using different nano-sized composites: a) for E and b) for PANAA / E.

### 3.4.2.3. Effect of initial conc. Of Hg(II)

One of the most important variables that can affect the adsorption process is initial heavy metal concentration. The effect of initial concentration of Hg(II) between (10-70) mg/L was studied on its adsorption onto  $\text{Al}_2\text{O}_3$  ( $\text{E}_{800}$ ) and PANAA / ( $\text{E}_{800}$ ) nanocomposites under previously determined optimum conditions and at room temperature. The results, in terms of removal efficiency versus initial concentration (mg/L), of Hg(II) ions are indicated in Fig. 17. It can be seen from the results that the percentage removal decreases with the increase in initial concentration, where it is seen that the adsorption of Hg (II) decreased gradually from 79% to 28% and 81.5% to 26.67% for  $\text{Al}_2\text{O}_3$  ( $\text{E}_{800}$ ) and PANAA / ( $\text{E}_{800}$ ), nanocomposites, respectively. Sufficient adsorption sites are available at lower initial concentrations, but at higher concentrations metal ions are greater than adsorption sites. Thus, it can be said that removal of mercury is concentration dependent using  $\text{Al}_2\text{O}_3$  ( $\text{E}_{800}$ ) and PANAA / ( $\text{E}_{800}$ ) nanocomposites particles as previously reported[81].

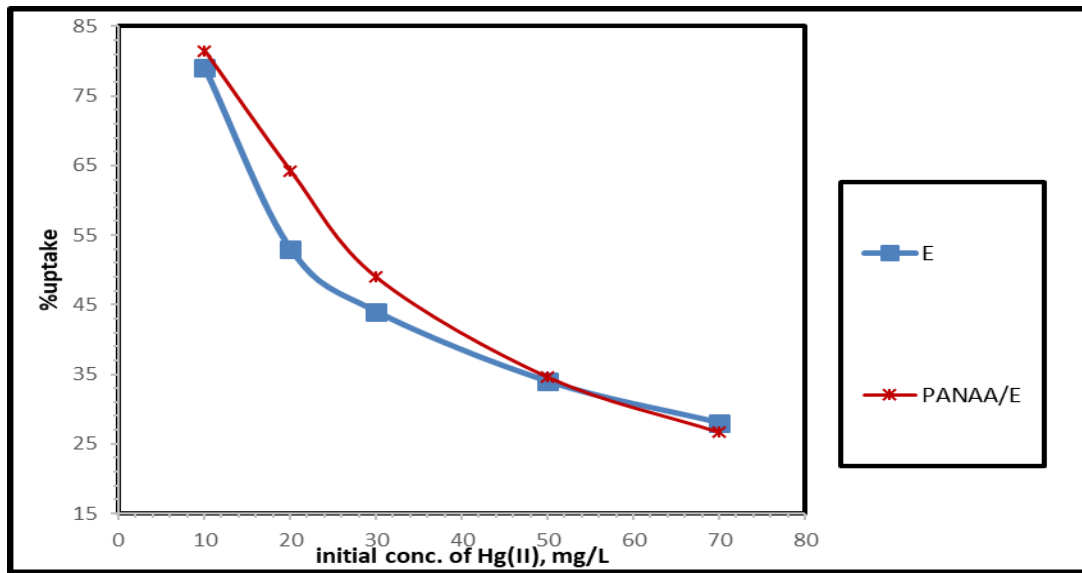


**Fig. 17.** Effect of initial concentration of Hg(II) removal percent using different nano-sized composites.

#### 3.4.2.4. Effect of adsorbent dose

The effect of adsorbent quantity of removal of Hg(II) is presented in Fig. 18. The removal of Hg(II) was investigated by adding various amount of adsorbent in the range of 0.025-0.1 g powder into a flask containing 50 ml of 20 ppm Hg(II) solution at pH= 9.43 and 9.53 for Al<sub>2</sub>O<sub>3</sub> (E<sub>800</sub>) and PANAA / (E<sub>800</sub>) nanocomposites particles. , respectively. Then stirring at rpm for 5h and 4h, in case of Al<sub>2</sub>O<sub>3</sub> (E<sub>800</sub>) and PANAA / (E<sub>800</sub>) nanocomposites particles, respectively. The results indicate that the adsorption of Hg (II) ions increases with increasing Al<sub>2</sub>O<sub>3</sub> (E<sub>800</sub>) and PANAA / (E<sub>800</sub>) nanocomposites particles mass due to the availability of the exchangeable active sites of the adsorbent particles.

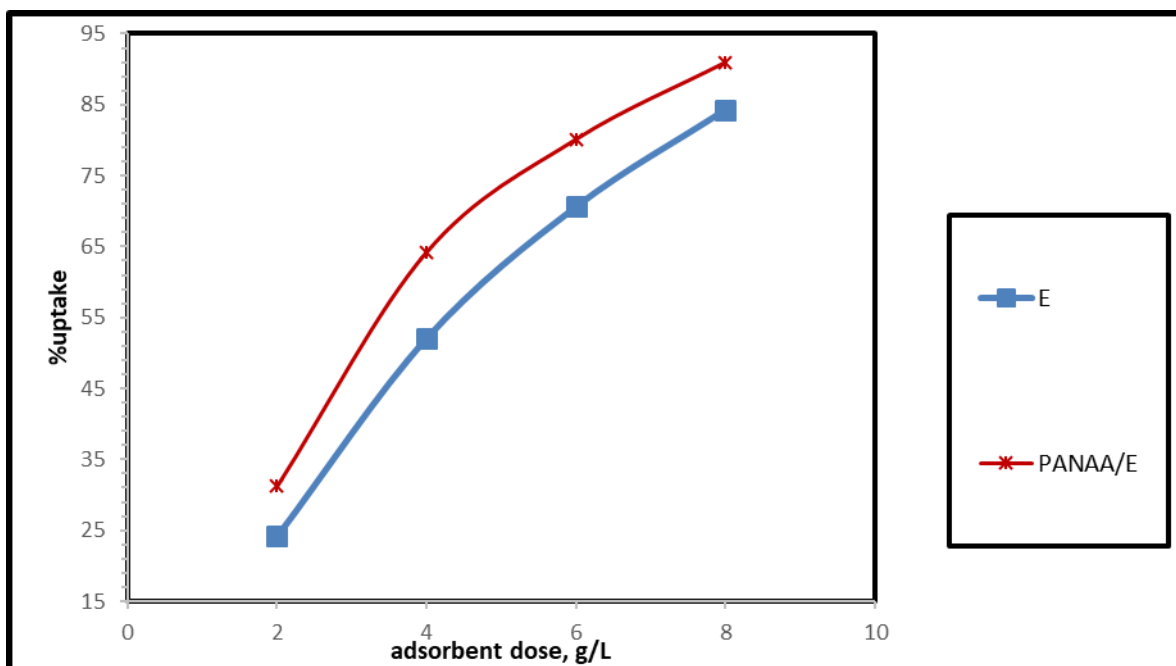


**Fig. 18.** Effect of adsorbent dose on Hg(II) removal percent using different nano-sized composites.

### 3.4.2.5. Effect of temperature

Temperature degree plays an important role which can affect the rate of adsorption process. The adsorption studies were carried out at three different temperatures (25, 35, 45 °C) separately for Hg(II) ions using 0.05 g for each adsorbent and Hg(II) concentration of 20 mg/L, at pH= 9.43 and 9.53 for Al<sub>2</sub>O<sub>3</sub> (E<sub>800</sub>) and PANAA / (E<sub>800</sub>) nanocomposites particles. , respectively. Then stirring at rpm for 5h and 4h, in case of Al<sub>2</sub>O<sub>3</sub> (E<sub>800</sub>) and PANAA / (E<sub>800</sub>) nanocomposites particles, respectively. The experimental results showed that the adsorption capacity decreased very slowly with increase in the solution temperature as shown in Fig. 19. This indicates that the adsorption of Hg(II) on the prepared adsorbents is an exothermic process. The decrease in the rate of adsorption with the increase in temperature may be attributed to the tendency of Hg(II) molecules to escape from the solid phase to bulk phase[81].

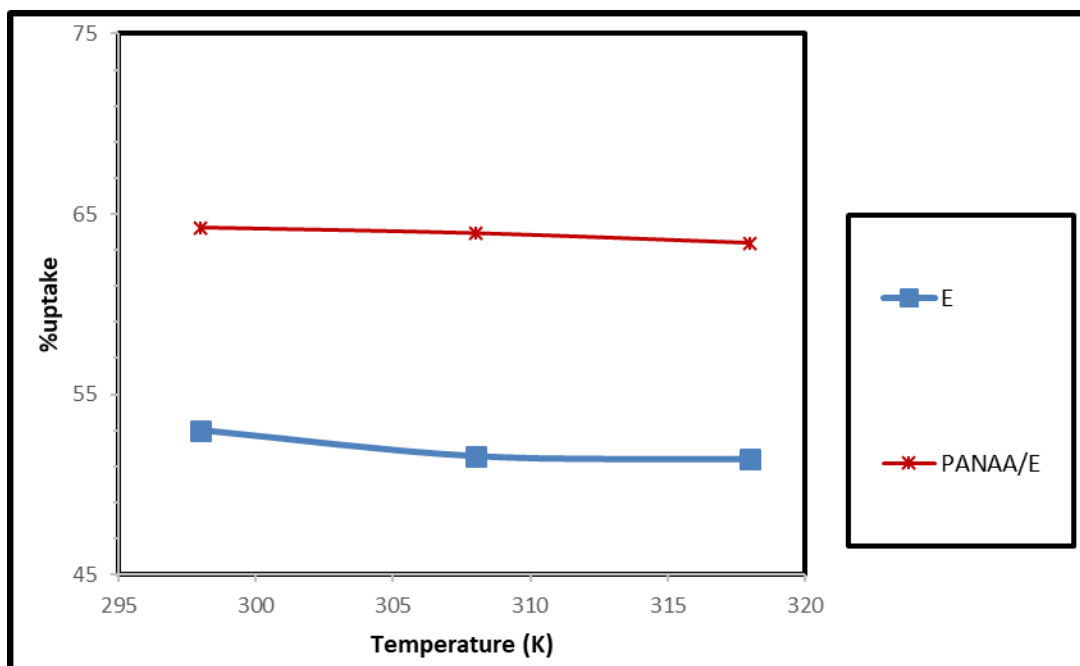


**Fig. 19.** Effect of temperature on Hg(II) removal percent using different nano-sized composites.

### **3.5. Adsorption kinetic study for adsorption of Hg(II) onto the surface of different adsorbents**

Adsorption kinetics studies are important in the treatment of aqueous effluents because they provide valuable information on the mechanism of the adsorption process. The metal adsorption mechanism can be explored by applying the pseudo-first-order and pseudo-second-order kinetic models. The pseudo-first-order kinetic model equation assumes that the binding is originated from a physical adsorption as follows[82]:

$$\log(q_e - qt) = \log q_e - \frac{K_1}{2.303} t \quad (11)$$

where  $q_e$  and  $q_t$  are the amount of heavy metal ions adsorbed on the adsorbent in mg (metal) /g (adsorbent) at equilibrium and at time  $t$ , respectively.  $K_1$  is the rate constant of first-order kinetics in  $\text{min}^{-1}$ . While the pseudo-second-order kinetic model is based on chemical adsorption (chemisorption) as follows[82].

$$\frac{t}{qt} = \frac{1}{K_2 q_e^2} + \frac{t}{q_e} \quad (12)$$

where  $q_e$  and  $q_t$  are the amount of heavy metal ions adsorbed by the adsorbent in mg (metal)/g (adsorbent) at equilibrium and at time  $t$ , respectively.  $K_2$  is the rate constant of second-order kinetics in  $\text{g} / (\text{mg}/\text{min})$ .

The values of  $K_1$  and  $K_2$  for different adsorbent were experimentally determined from Eqs. (11 and 12), respectively.

### 3.5.1. Adsorption kinetic study for adsorption of Hg(II) onto the surface of Al<sub>2</sub>O<sub>3</sub> (E<sub>800</sub>)

The fitting curves obtained from the linear plots of  $\log (q_e - q_t)$  versus time and  $(t/q_t)$  versus time are plotted in Fig. 20 and 21, respectively. The values of  $K_1$  and  $K_2$  for different adsorbent were experimentally determined from Eqs. (11 and 12), respectively. From Fig. 20 and Fig. 21, it appears that the second order model seems to be more favorable for Hg(II) sorption process indicating its chemical adsorption by Al<sub>2</sub>O<sub>3</sub> (E<sub>800</sub>) nanocomposite. The  $q_e$  values experimental from pseudo-first-ordered kinetic model were too small compared the calculated value for Hg(II). However, the experimental value  $q_e$  from pseudo-second-order kinetic model were close to the calculated value. These results suggested that pseudo second-order adsorption mechanism is predominate and that the overall rate of the Hg(II) adsorption process appeared to be controlled by the chemisorption process[83]. The obtained  $k_1$  and  $k_2$  values for Al<sub>2</sub>O<sub>3</sub> (E<sub>800</sub>) nanocomposite plus other parameters obtained from the linear form of pseudo-first-order and pseudo-second-order are listed in Table 3.

Al <sub>2</sub> O <sub>3</sub> (E <sub>800</sub> )	Pseudo-first-ordered model			Pseudo-second-ordered model		
$q_e$ (cal) (mg/g)	$q_e$ (exp) (mg/g)	$K_1$	$R^2$	$q_e$ (exp) (mg/g)	$K_2$	$R^2$
10.6	1.655	0.0018	0.4206	10.74	0.0025	0.9983

Table 3. pseudo-first-order and pseudo-second-order reaction rate models parameters for adsorption of Hg(II) on Al<sub>2</sub>O<sub>3</sub> (E<sub>800</sub>) nanocomposite.

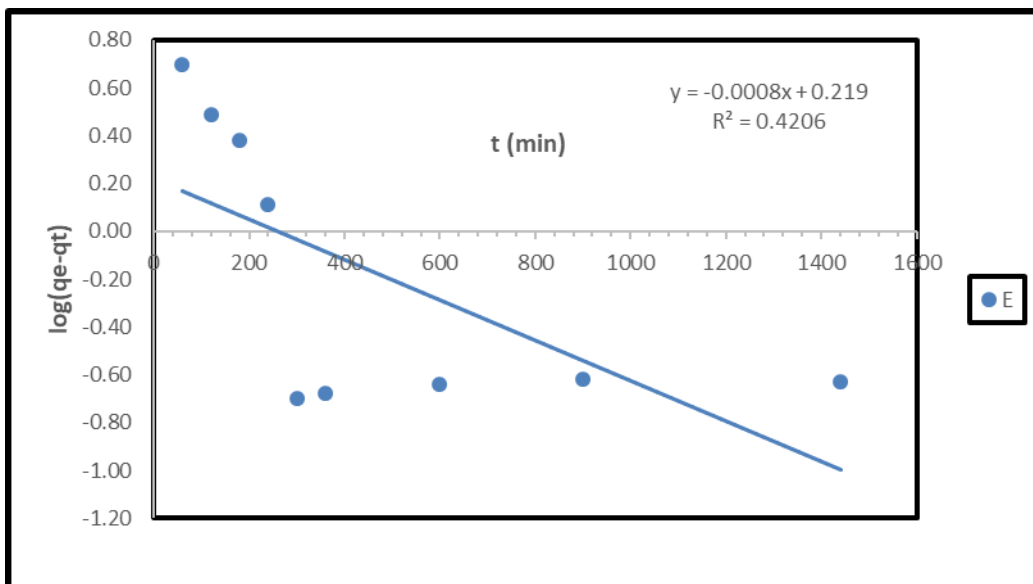


**Fig. 20.** Pseudo-first-order plots for adsorption of Hg(II) on  $\text{Al}_2\text{O}_3$  ( $\text{E}_{800}$ ) nanocomposite.

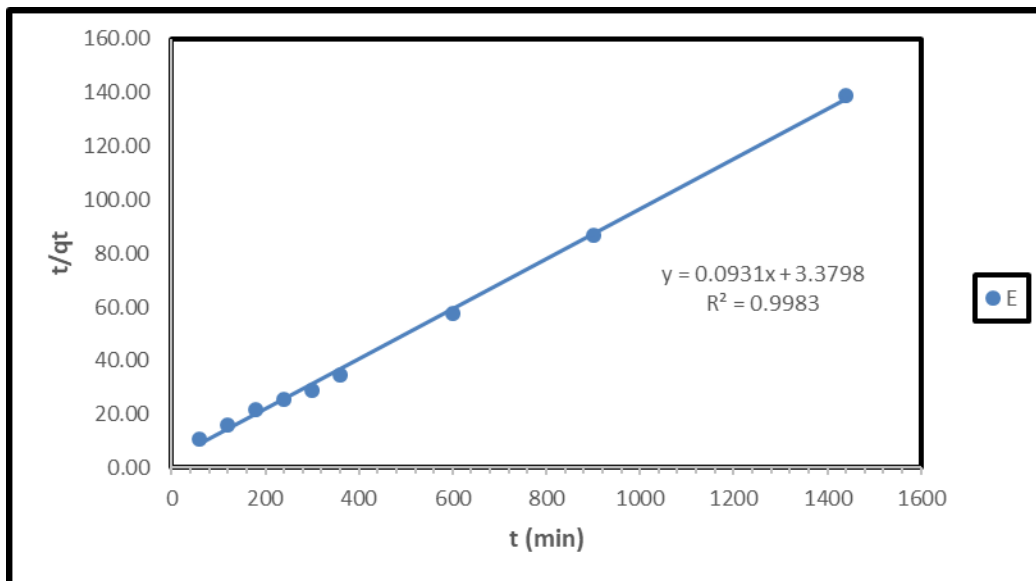


**Fig. 21.** Pseudo-second-order plots for adsorption of Hg(II) on  $\text{Al}_2\text{O}_3$  ( $\text{E}_{800}$ ) nanocomposite.

**3.5.2. Adsorption kinetic study for adsorption of Hg(II) onto the surface of PANAA /Al<sub>2</sub>O<sub>3</sub> (E<sub>800</sub>)**

The fitting curves obtained from the linear plots of  $\log (q_e - q_t)$  versus time and  $(t/q_t)$  versus time are plotted in Fig. 22 and 23, respectively. The values of  $K_1$  and  $K_2$  for different adsorbent were experimentally determined from Eqs. (11 and 12), respectively. From Fig. 22 and Fig. 23, it appears that the second order model seems to be more favorable for Hg(II) sorption process indicating its chemical adsorption by PANAA /Al<sub>2</sub>O<sub>3</sub> (E<sub>800</sub>) nanocomposite. The  $q_e$  values experimental from pseudo-first-ordered kinetic model were too small compared the calculated value for Hg(II). However, the experimental value  $q_e$  from pseudo-second-order kinetic model were close to the calculated value. These results suggested that pseudo second-order adsorption mechanism is predominate and that the overall rate of the Hg(II) adsorption process appeared to be controlled by the chemisorption process[83]. The obtained  $k_1$  and  $k_2$  values for Al<sub>2</sub>O<sub>3</sub> (E<sub>800</sub>) nanocomposite plus other parameters obtained from the linear form of pseudo-first-order and pseudo-second-order are listed in Table 4.

PANAA / (E <sub>800</sub> )	Pseudo-first-ordered model			Pseudo-second-ordered model		
$q_e$ (cal) (mg/g)	$q_e$ (exp) (mg/g)	$K_1$	$R^2$	$q_e$ (exp) (mg/g)	$K_2$	$R^2$
12.85	1.22	0.0039	0.3754	13.19	0.0027	0.9983

Table 4. pseudo-first-order and pseudo-second-order reaction rate models parameters for adsorption of Hg(II) on PANAA /Al<sub>2</sub>O<sub>3</sub> (E<sub>800</sub>) nanocomposite.

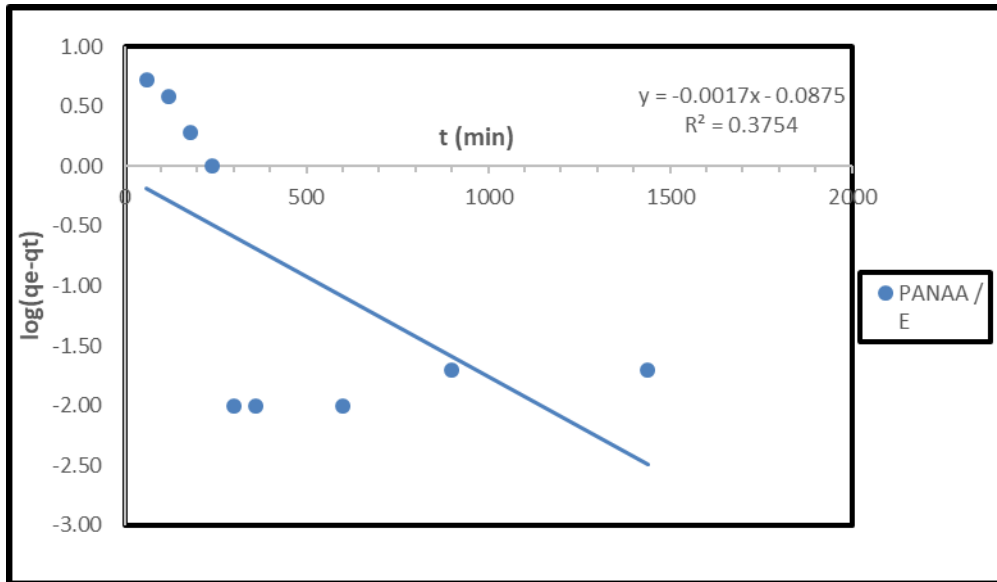


**Fig. 22.** Pseudo-first-order plots for adsorption of Hg(II) on PANAA /Al<sub>2</sub>O<sub>3</sub> (E<sub>800</sub>) nanocomposite.

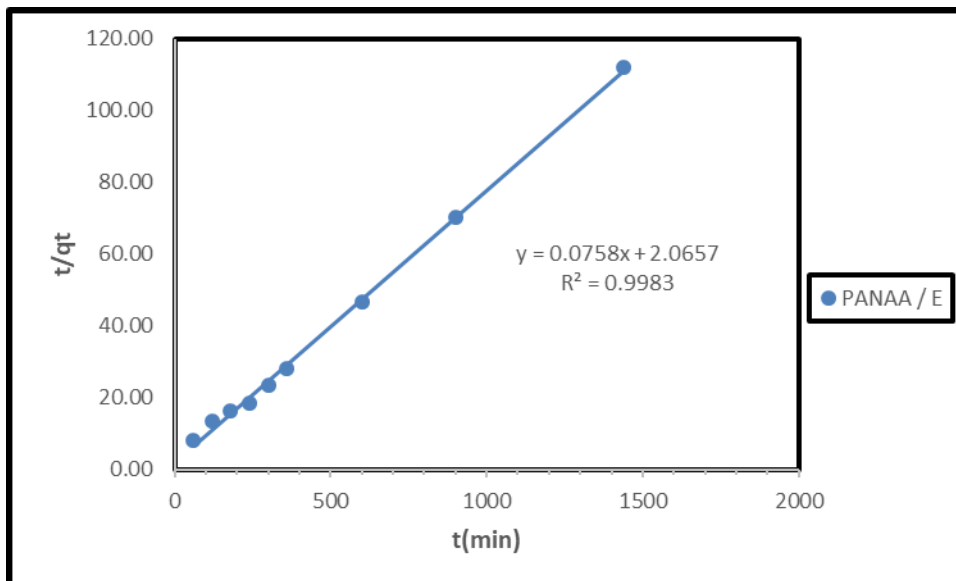


**Fig. 23.** Pseudo-second-order plots for adsorption of Hg(II) on PANAA /Al<sub>2</sub>O<sub>3</sub> (E<sub>800</sub>) nanocomposite.

However, to gain further insight into the rate determining step involved in the adsorption of Hg(II) on different adsorbents, intra-particle diffusion model was examined by applying the Weber and Morris equation (13):

$$q_t = C + K_i t^{0.5} \quad (13)$$

where  $K_i$  is the intra-particle diffusion constant ( $\text{mg g}^{-1} \text{min}^{-0.5}$ ), and  $C$  represents the boundary layer thickness ( $\text{mg g}^{-1}$ ). According to this model, plotting of  $q_t$  against  $t^{0.5}$  values should give a straight line which passes through the origin, if the rate determining step is the intra-particle diffusion. Otherwise, boundary layer diffusion or chemical reaction is the rate determining step. In the current case, the obtained plots Fig. 24(a,b) is a multilinear or not passing the origin which indicates that the overall adsorption process may be proceed by more than one mechanism such as film diffusion, chemical reaction, and intra-particle diffusion[84].

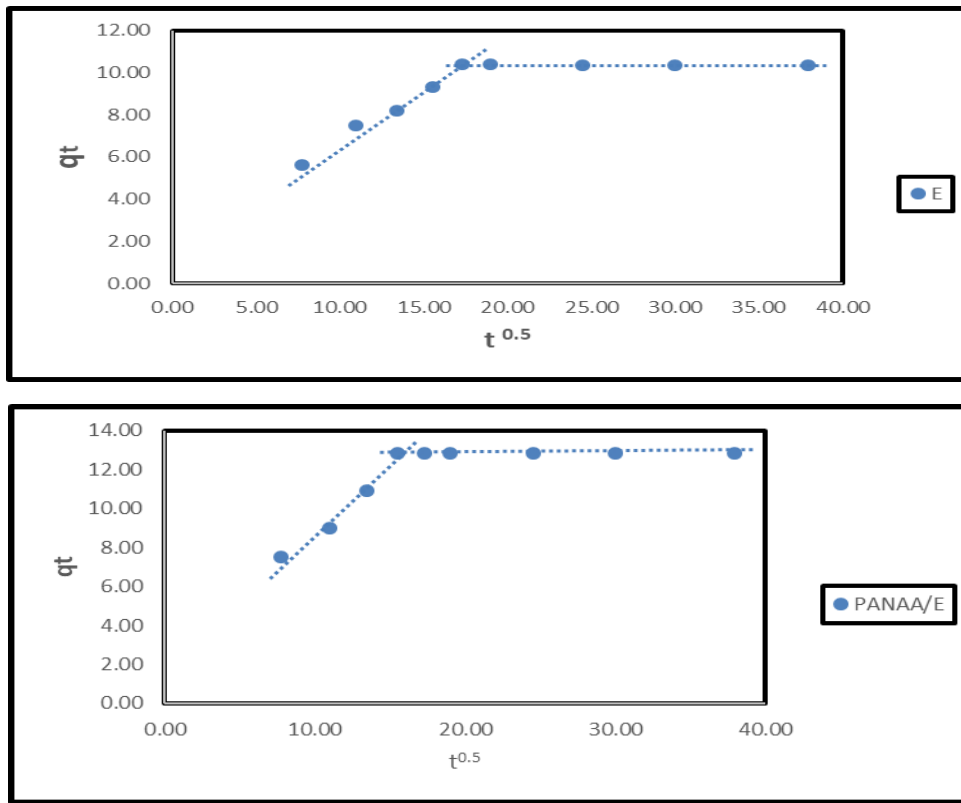


**Fig. 24(a,b).** Intra-particle diffusion model for adsorption of Hg(II) onto a) Al<sub>2</sub>O<sub>3</sub> (E<sub>800</sub>), b) PANAA /[Al<sub>2</sub>O<sub>3</sub> (E<sub>800</sub>)].

### **3.6. Adsorption isotherms (Equilibrium modeling)**

#### **3.6.1. Adsorption isotherm for adsorption of Hg(II) onto the prepared nanosized particles**

The equilibrium relationship between the quantity of adsorbate per unit of adsorbent ( $q_e$ ) and its equilibrium solution concentration ( $C_e$ ) at a constant temperature is known as the adsorption isotherm. And it is very important to the design of adsorption processes[85]. Several isotherm models have been developed for evaluating the equilibrium adsorption of compounds from solutions such as Langmuir, Freundlich, Dubinin-Radushkevich and Temkin, etc. since the more common models used to investigate the adsorption isotherm are Langmuir, Freundlich and Temkin isotherm models, the experimental results of this study were fitted with these three models.

##### **3.6.1.1. Langmuir isotherm model**

The common isotherm models (Langmuir and Freundlich), were used to describe the adsorption of Hg (II) ion on the nano-particles. Langmuir model supposed that all the adsorption sites of the adsorbent have the same binding energy and every site joints to only one adsorbate[86]. This model of isotherm assumes the formation of a monolayer adsorbate on the outer surface of the adsorbent, and after that no further adsorption takes place. It is valid for monolayer adsorption onto a surface containing a finite number of identical sites.it assumes uniform energies of adsorption onto the surface and no transmigration of adsorbate in the plane of the surface. The linearized Langmuir isotherm is given by Eq. (14):

$$\frac{C_e}{q_e} = \frac{b}{qm} + \frac{1}{qm} C_e \quad (14)$$

where  $q_e$  is the equilibrium adsorption capacity of the adsorbent in mg (metal)/g (adsorbent),  $C_e$  is the equilibrium concentration of Hg(II) ions in (mg/L),  $q_m$  is the maximum amount of metal adsorbed in mg (metal)/g (adsorbent), and  $b$  is the Langmuir constant that belongs to the bonding energy of adsorption in (L/mg). Linear plot of  $C_e/q_e$  versus  $C_e$  shows Langmuir isotherm Fig. 25(a,b). values of  $q_m$  and  $b$  were calculated from the slop and intercept of the linear plots and are presented in Table 5. The essential characteristics of Langmuir isotherm can be expressed by a dimensionless constant called equilibrium parameters  $R_L$ , defined as:

$$RL = \frac{1}{1+bC_0} \quad (15)$$

Where  $b$  is the Langmuir constant and  $C_0$  is the primary Hg(II) concentration (mg/L),  $R_L$  value indicates the adsorption nature to be either unfavorable if  $RL > 1$ , Linear if  $R_L=1$ , favorable if  $0 < R_L < 1$  and irreversible if  $R_L=0$  [86]. Table 5. Shows  $R_L$  values between zero and one, which indicate favorable adsorption.

Adsorbent	Langmuir isotherm parameters					
	$R^2$	Slope	Intercept	$q_m$ (mg/g)	$b$ (L/mg)	$R_L$
$Al_2O_3$	0.982	0.048	0.3525	21.01	7.4	0.0133
PANAA/ $Al_2O_3$	0.997	0.051	0.1941	19.72	3.826	0.0254

Table 5. Langmuir isotherm parameters for adsorption of Hg(II) on different prepared nanoparticles.

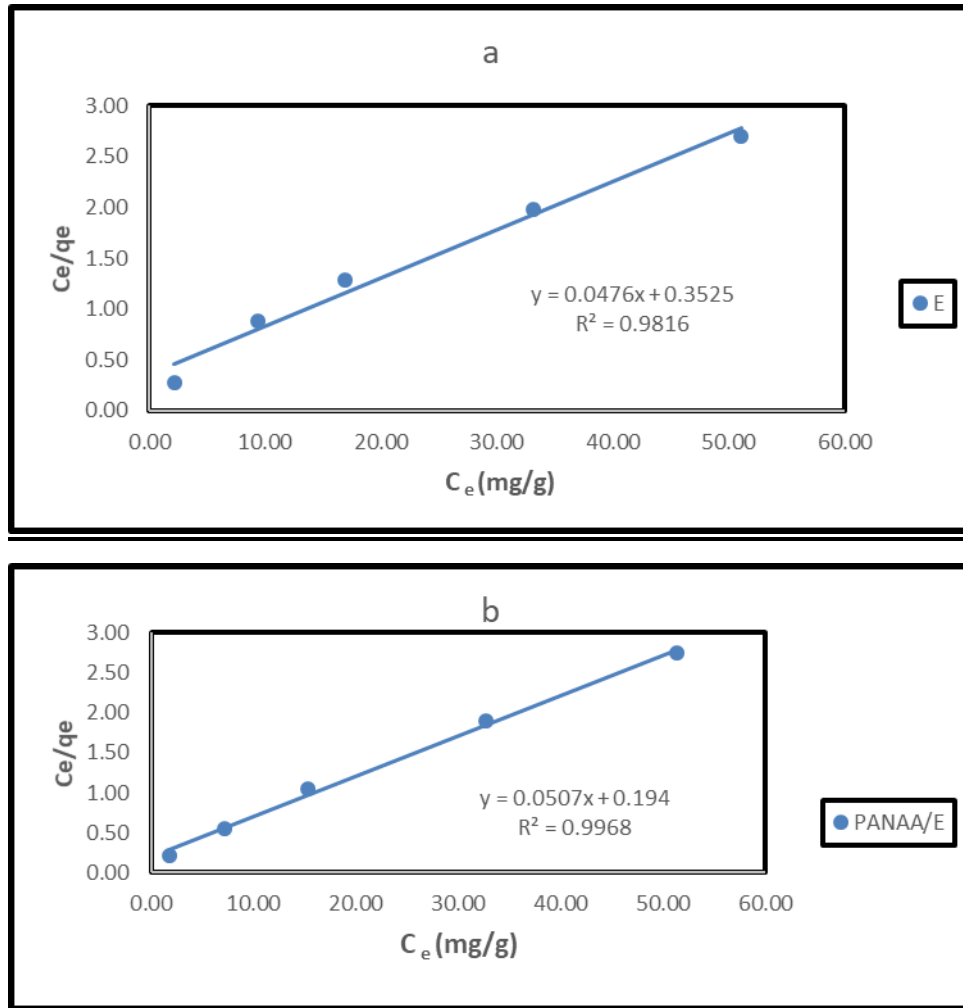


**Fig. 25(a,b).** Langmuir isotherm model for Hg(II) adsorption on different nano-sized composites: a) for E, and b) for PANAA/ (E).

### 3.6.1.2. Freundlich isotherm model

This model is used to describe the adsorption characteristics for the heterogeneous surface[86]. it assumes heterogeneity of binding energies of adsorption sites. The linearized Freundlich isotherm is given by Eq. (16):

$$\ln q_e = \ln K_f + \left(\frac{1}{n}\right) \ln C_e \quad (16)$$

where  $q_e$  is the equilibrium adsorption capacity of the adsorbent in mg (metal)/g (adsorbent),  $C_e$  is the equilibrium concentration of heavy metal ions in (mg/L),  $K_f$  is

the constant refers to the adsorption capacity of the adsorbent in (mg/L), and  $n$  is the constant linked to the adsorption intensity.  $(1/n)$  is the heterogeneity factor and it is a function of the strength of adsorption in the adsorption process. If  $n=1$  (i.e.  $(1/n)=1$ ), the partition between the two phases are independent of the concentration. If value of  $1/n$  is below one, it indicates a normal adsorption. On the other hand,  $1/n$  being above one indicates cooperative adsorption. In addition to, the linear least squares method and the linearly transformed equations have been widely applied to correlate sorption data where the smaller  $1/n$ , the greater the expected heterogeneity. This expression reduces to a linear adsorption isotherm when  $1/n = 1$ . If  $n$  lies between one and ten, this indicates a favorable sorption process[87]. When  $\ln q_e$  is plotted against  $\ln C_e$  and the data are treated by linear regression analysis, as shown in Fig. 26 (a,b) for Hg(II) adsorption on different nano-sized composites,  $1/n$ ,  $K_f$  constants are determined from the slope and intercept. The data presented in Table 6, showing the values of  $1/n$  and  $n$  which indicates that the sorption of Hg(II) onto the prepared nano-sized particles is favorable.

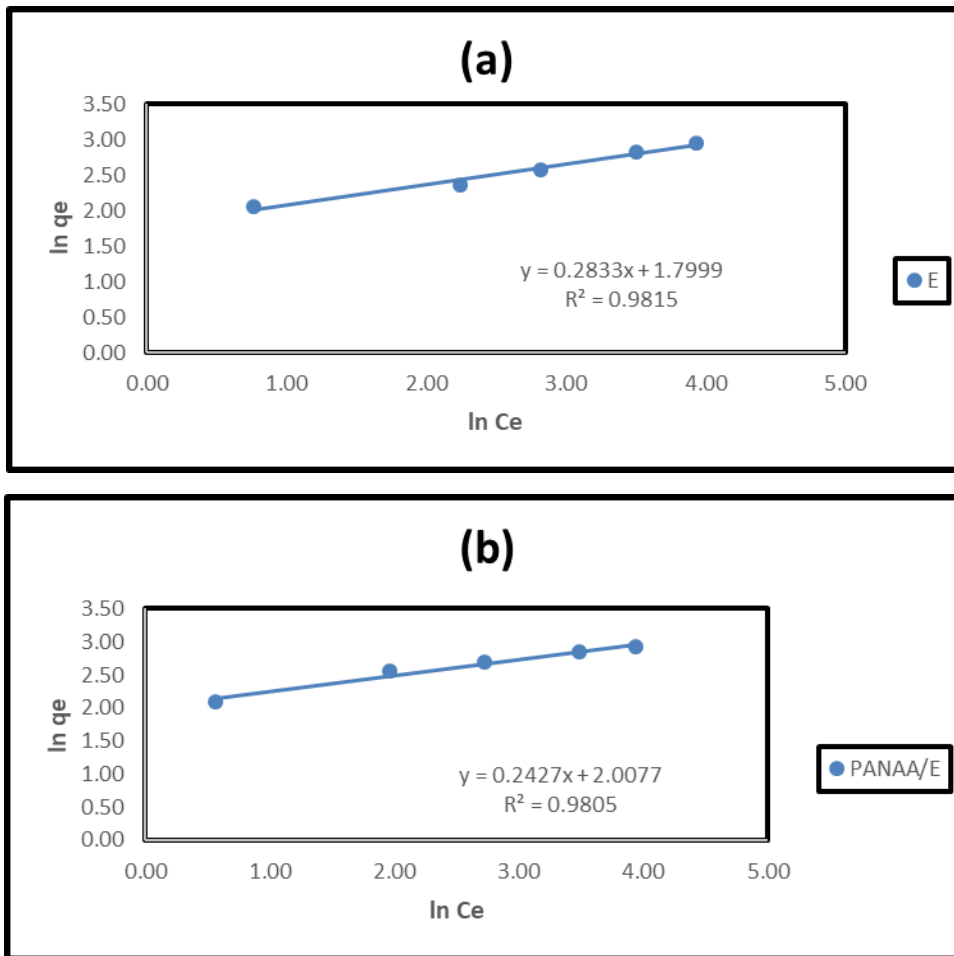


**Fig. 26(a,b).** Freundlich isotherm model for Hg(II) adsorption on different nano-sized composites: a) for E, and b) for PANAA/ E.

Adsorbent	Freundlich isotherm Parameters					
	Slope	Intercept	K <sub>f</sub>	1/n	n	R <sup>2</sup>
Al <sub>2</sub> O <sub>3</sub>	0.2833	1.7999	6.0490	0.2833	3.5298	0.9815
PANAA/Al <sub>2</sub> O <sub>3</sub>	0.2427	2.0077	7.4460	0.2427	4.1201	0.9805

**Table 6. Freundlich isotherm parameters for adsorption of Hg(II) on different prepared nanosized particles.**

Usually, for the valuation of preeminent fit, values of correlation coefficients (R<sup>2</sup>) of linear plots of the three models are compared. Based on the three model constants and their correlation coefficients it can be concluded that adsorption of Hg(II) on Al<sub>2</sub>O<sub>3</sub>(E<sub>800</sub>) and PANAA / Al<sub>2</sub>O<sub>3</sub>(E<sub>800</sub>) adsorbents is best described by Langmuir adsorption isotherm since it has the closest R<sup>2</sup> to the unity value, plus Langmuir isotherm model generated the nearest calculated maximum adsorption capacity to the experimentally obtained one. This, therefore, suggests that adsorption occurs as a monolayer adsorbate on the outer surface of the adsorbent.

### **3.6.1.3. Temkin isotherm model**

This model of isotherm includes a factor that explicitly taking into the account of adsorbent-adsorbate interactions. The model supposes that heat of adsorption (function of temperature) of all molecules in the layer would reduce linearly rather than logarithmic with coverage[88, 89]. As indicated in the equation (17) its linearized form Eq. (18), its derivation is characterized by a uniform distribution of binding energies (up to some maximum binding energy).

$$q_e = \frac{RT}{b} \ln (K_T \cdot C_e) \quad (17)$$

This equation can be linearized as following:

$$q_e = B \ln(K_T) + B \ln (C_e) \quad (18)$$

Where  $B = \frac{RT}{b}$

The adsorption data can be examined according to the previous equation. A plot of  $q_e$  versus  $\ln C_e$  enables the determination of the isotherm constant  $K_T$  and  $B$  as shown in Fig. 27 (a-f),  $K_T$  is the equilibrium binding constant (L/mg) corresponding to the maximum binding energy and constant  $B$  is related to the heat of adsorption ( $J.mol^{-1}$ ).  $R$  is the universal gas constant ( $8.314 J/mol.k$ ).  $B$  is also a Temkin isotherm constant while  $T$  is the absolute temperature (T) in Kelvin. The values of these parameters are presented in Table. 7. Based on the values of  $R^2$ (correlation coefficient), it could be concluded that Temkin isotherm model is applicable to some degree for the adsorption of Hg (II) onto the prepared nano-sized materials.

Adsorbent	Temkin isotherm Parameters						
	Slope	Intercept	$\ln K_T$ (L/mg)	$K_T$ (L/mg)	$B$	$b$ (J/mol)	$R^2$
$Al_2O_3$	3.51	4.14	1.18	3.25	3.51	0.71	0.939
PANAA/ $Al_2O_3$	3.09	6.50	2.11	8.22	3.09	0.80	0.998

**Table 7. Temkin isotherm parameters for adsorption of Hg(II) on different prepared nanosized particles.**

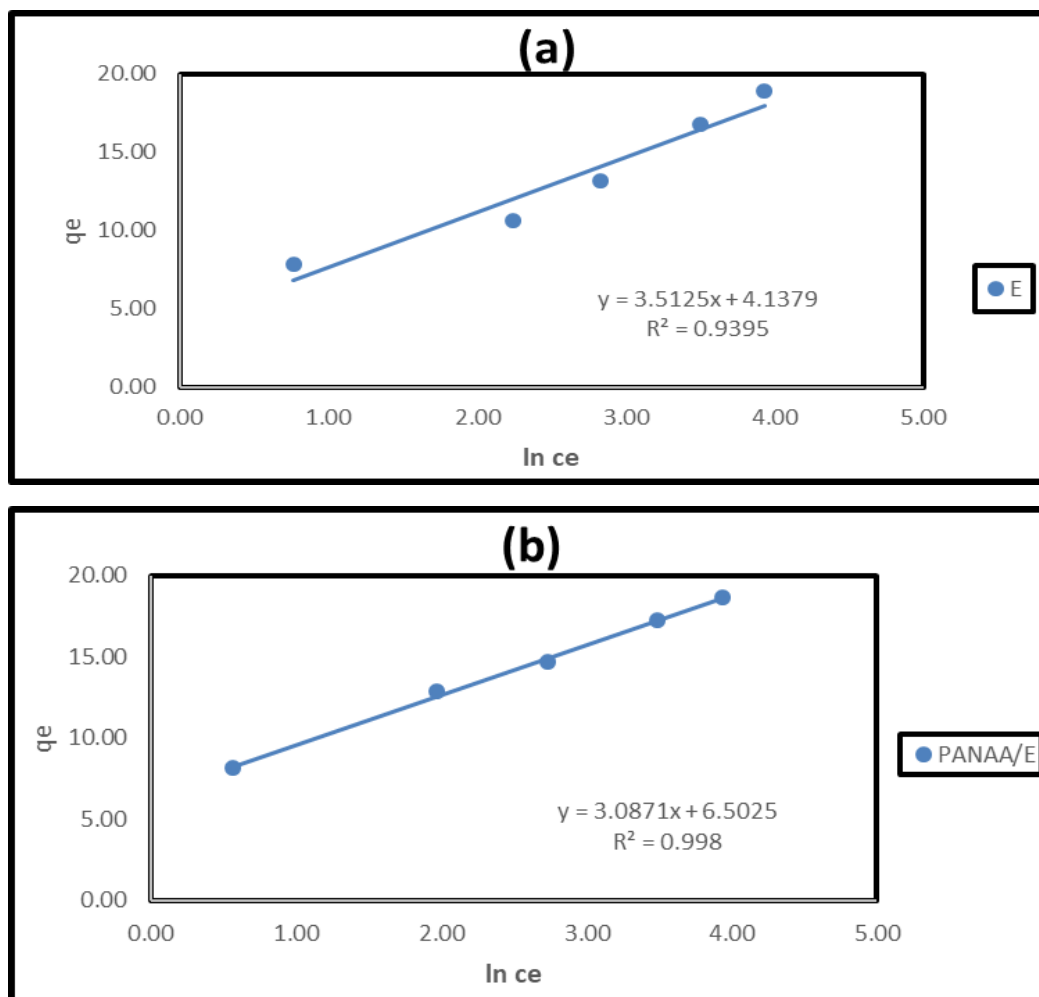


**Fig. 27(a,b).** Temkin isotherm model for Hg(II) adsorption on different nano-sized composites: a) for E, and b) for PANAA/ E.

### **3.6.2. Thermodynamic studies for adsorption of Hg(II) on different prepared nano- particles**

The effect of adsorption media temperatures on the adsorption of Hg(II) on the as-prepared adsorbents was explored in the range of 298-318 K under the adsorption conditions: 0.05 g adsorbent, 20 mg/L initial concentration of metal ion, 400 rpm stirring rate and apply other optimum condition for each adsorbent. The results exhibited that the adsorption capacity, as shown previously in Fig. 19. indicates that the adsorption capacity of Hg(II) on each adsorbent is an exothermic

nature of the adsorption process. The decrease in the rate of adsorption with the increase of the temperature can be attributed to the low tendency of Hg (II) molecules to the solid phase at high temperature. The values of thermodynamic parameters such as change in enthalpy ( $\Delta H^\circ$ ), change in entropy ( $\Delta S^\circ$ ) and change in free energy ( $\Delta G^\circ$ ), were determined by using the following Van's Hoff equation[90]:

$$\ln K_c = \Delta S^\circ/R - \Delta H^\circ/RT \quad (19)$$

where  $K_c = C_{Ae}/C_e$

$K_c$  is the equilibrium constant,  $C_{Ae}$  is the solid phase concentration at equilibrium (mg/L),  $T$  is the temperature in Kelvin and  $R$  is the gas constant. By plotting  $\ln K_c$  against  $1/T$  gives a straight line with a slope and intercept equal to ( $-\Delta H^\circ/R$ ) and  $\Delta S^\circ/RT$ , respectively. The values of  $\Delta H^\circ$  and  $\Delta S^\circ/R$  were calculated from Fig. 28 (a,b) and reported in Table 8. The negative values of  $\Delta H^\circ$  indicate the exothermic nature of adsorption process for Hg(II) on all prepared adsorbents. The positive values of entropy changes  $\Delta S^\circ$  corresponds on an increase in degree of freedom of the adsorbed species. Gibbs free energy  $\Delta G^\circ$  of adsorption was calculated from the following relations and the values are given in Table 8.

$$(\Delta G^\circ) = -RT \ln K_c \quad (20)$$

$$(\Delta G^\circ) = \Delta H^\circ - T\Delta S^\circ \quad (21)$$

The negative values of ( $\Delta G^\circ$ ) indicated that the adsorption of Hg(II) on the different adsorbents is a spontaneous process and the decrease in ( $\Delta G^\circ$ ) values with increasing the temperature indicates that the adsorption process is more preferable at higher temperature for all adsorbents.

Adsorbent	Temperature (K)	lnK <sub>c</sub>	ΔG° (KJ/mol)	ΔH° (KJ/mol)	ΔS° (KJ/mol.k)
Al <sub>2</sub> O <sub>3</sub>	298	0.0820	-0.203	-0.1428	0.0002
	308	0.0792	-0.204		
	318	0.0784	-0.207		
PANAA/Al <sub>2</sub> O <sub>3</sub>	298	0.5862	-1.4524	-1.4455	0.00037
	308	0.5727	-1.4666		
	318	0.5494	-1.4725		

**Table 8.** Thermodynamic parameters for the adsorption of Hg(II) on all prepared adsorbents.

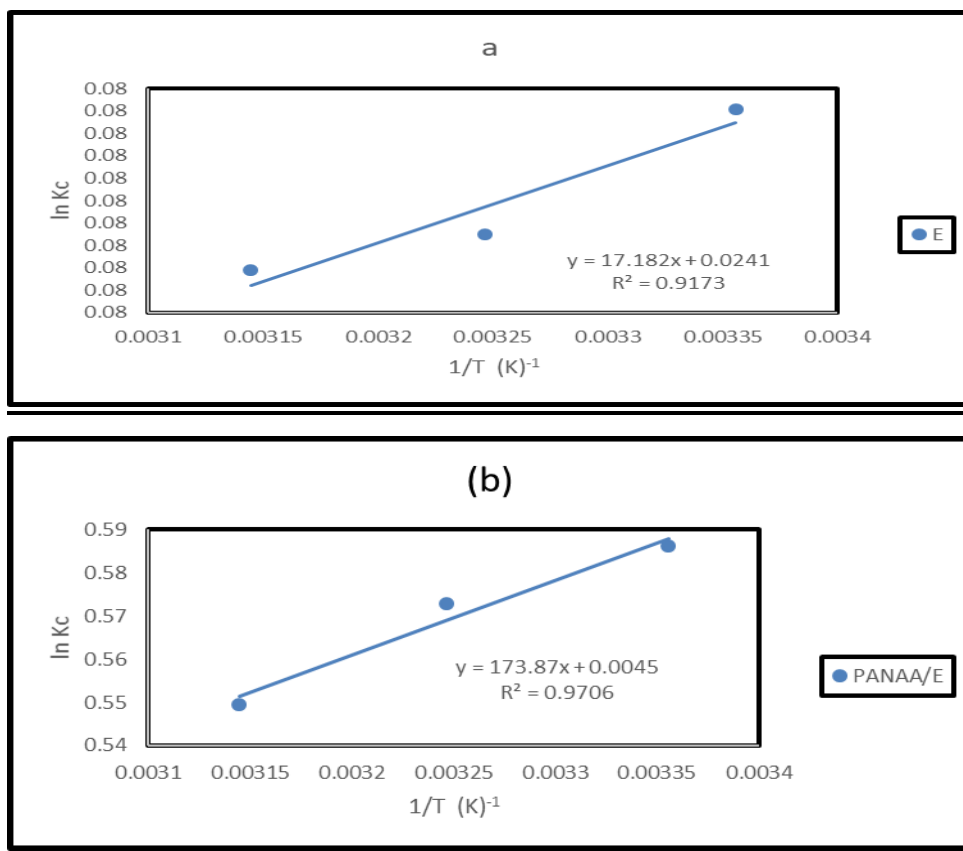


**Fig. 28(a,b).** Plots of ln K<sub>c</sub> against 1/T for Hg(II) adsorption on different nano-sized composites: a) for E, and b) for PANAA/ E.

#### **4. Conclusion**

A facile nanocomposite of poly (aniline-CO-O-anthranilic acid) (PANAA/ Al<sub>2</sub>O<sub>3</sub>) was synthesized via chemical oxidative polymerization of anthranilic acid and aniline co-monomers at equimolar ratios (1:1) with the Al<sub>2</sub>O<sub>3</sub> nanostructure. A proposed mechanism for nanocomposite formation was suggested and the structure of the as-prepared adsorbents was characterized by FT-IR, SEM, TEM and XRD techniques. The nanocomposite was then utilized as an effective adsorbent for the removal of Hg(II) ions. The kinetics and isotherm modelling studies showed that the experimental data fitted well with the pseudo-second-order and Langmuir isotherm models, respectively. The maximum capacity of the adsorbent was found to be 19.72 mg g<sup>-1</sup> for Hg(II). All obtained results depict that the modified PANAA/ Al<sub>2</sub>O<sub>3</sub> nanocomposite can be used as an effective, easily separable, and reusable adsorbent for the removal of toxic Hg(II) from aqueous solutions.

#### **Declaration of Interest**

Hesham H. El-Feky, declares that he has no conflict of interest. Mostafa Y. Nassar, declares that he has no conflict of interest. Alaa S. Amin, declares that he has no conflict of interest.

**Ethical Approval** This article does not contain any studies with human participants or animals performed by any of the authors.

**Informed Consent** Informed consent is not applicable to this study.

## References

1. Yadav, V.B., R. Gadi, and S. Kalra, *Clay based nanocomposites for removal of heavy metals from water: a review*. Journal of environmental management, 2019. **232**: p. 803-817.
2. Sun, Q., et al., *Elaborate design of polymeric nanocomposites with Mg (ii)-buffering nanochannels for highly efficient and selective removal of heavy metals from water: case study for Cu (ii)*. Environmental Science: Nano, 2018. **5**(10): p. 2440-2451.
3. Sajid, M., et al., *Removal of heavy metals and organic pollutants from water using dendritic polymers based adsorbents: a critical review*. Separation and Purification Technology, 2018. **191**: p. 400-423.
4. Joseph, L., et al., *Removal of heavy metals from water sources in the developing world using low-cost materials: A review*. Chemosphere, 2019.
5. Al-Mallah, Z. and A.S. Amin, *Utility of solid phase extraction for colorimetric determination of lead in waters, vegetables, biological and soil samples*. Journal of Industrial and Engineering Chemistry, 2018. **67**: p. 461-468.
6. Belayutham, S., V.A. González, and T.W. Yiu, *The dynamics of proximal and distal factors in construction site water pollution*. Journal of Cleaner Production, 2016. **113**: p. 54-65.
7. Fiyadh, S.S., et al., *Review on heavy metal adsorption processes by carbon nanotubes*. Journal of Cleaner Production, 2019.
8. Mahmoud, M.E., et al., *Water and soil decontamination of toxic heavy metals using aminosilica-functionalized-ionic liquid nanocomposite*. Journal of Molecular Liquids, 2018. **266**: p. 834-845.
9. Lingamdinne, L.P., et al., *Process optimization and adsorption modeling of Pb (II) on nickel ferrite-reduced graphene oxide nano-composite*. Journal of Molecular Liquids, 2018. **250**: p. 202-211.
10. Shang, Z., et al., *Removal of Pb (II), Cd (II) and Hg (II) from aqueous solution by mercapto-modified coal gangue*. Journal of environmental management, 2019. **231**: p. 391-396.
11. Chandra, V. and K.S. Kim, *Highly selective adsorption of Hg 2+ by a polypyrrole-reduced graphene oxide composite*. Chemical Communications, 2011. **47**(13): p. 3942-3944.
12. Hadi, P., et al., *Aqueous mercury adsorption by activated carbons*. Water Research, 2015. **73**: p. 37-55.
13. Howie, M.G., A.K. Jackson, and D.A. Cristol, *Spatial extent of mercury contamination in birds and their prey on the floodplain of a contaminated river*. Science of The Total Environment, 2018. **630**: p. 1446-1452.
14. Inbaraj, B.S., et al., *Adsorption of toxic mercury (II) by an extracellular biopolymer poly ( $\gamma$ -glutamic acid)*. Bioresource Technology, 2009. **100**(1): p. 200-207.
15. Jose, A. and J.G. Ray, *Toxic heavy metals in human blood in relation to certain food and environmental samples in Kerala, South India*. Environmental Science and Pollution Research, 2018. **25**(8): p. 7946-7953.
16. Kopec, A.D., et al., *Elevated mercury in blood and feathers of breeding marsh birds along the contaminated lower Penobscot River, Maine, USA*. Science of The Total Environment, 2018. **634**: p. 1563-1579.
17. Martinez, G., et al., *Mercury contamination in riverine sediments and fish associated with artisanal and small-scale gold mining in Madre de Dios, Peru*. International journal of environmental research and public health, 2018. **15**(8): p. 1584.
18. Nakayama, S.F., et al., *Blood mercury, lead, cadmium, manganese and selenium levels in pregnant women and their determinants: the Japan Environment and Children's Study (JECS)*. Journal of exposure science & environmental epidemiology, 2019. **29**(5): p. 633-647.

19. Rahman, Z. and V.P. Singh, *The relative impact of toxic heavy metals (THMs)(arsenic (As), cadmium (Cd), chromium (Cr)(VI), mercury (Hg), and lead (Pb)) on the total environment: an overview*. Environmental monitoring and assessment, 2019. **191**(7): p. 419.
20. Zhao, Z.-Q., et al., *Selective adsorption toward toxic metal ions results in selective response: electrochemical studies on a polypyrrole/reduced graphene oxide nanocomposite*. Chemical Communications, 2012. **48**(16): p. 2180-2182.
21. Wang, L.K. and H. Yung-Tse, *a Nazih K SHAMMAS*. Physicochemical treatment processes, 2005.
22. Nassar, M.Y. and I.S. Ahmed, *Template-free hydrothermal derived cobalt oxide nanopowders: synthesis, characterization, and removal of organic dyes*. Materials Research Bulletin, 2012. **47**(9): p. 2638-2645.
23. Nassar, M.Y., E.I. Ali, and E.S. Zakaria, *Tunable auto-combustion preparation of TiO<sub>2</sub> nanostructures as efficient adsorbents for the removal of an anionic textile dye*. RSC advances, 2017. **7**(13): p. 8034-8050.
24. Chen, Q., et al., *Comparison of heavy metal removals from aqueous solutions by chemical precipitation and characteristics of precipitates*. Journal of water process engineering, 2018. **26**: p. 289-300.
25. Matlock, M.M., B.S. Howerton, and D.A. Atwood, *Chemical precipitation of heavy metals from acid mine drainage*. Water research, 2002. **36**(19): p. 4757-4764.
26. Bashir, A., et al., *Removal of heavy metal ions from aqueous system by ion-exchange and biosorption methods*. Environmental Chemistry Letters, 2019. **17**(2): p. 729-754.
27. Dong, Q., et al., *Selective removal of lead ions through capacitive deionization: Role of ion-exchange membrane*. Chemical Engineering Journal, 2019. **361**: p. 1535-1542.
28. Awad, F.S., et al., *Effective removal of mercury (II) from aqueous solutions by chemically modified graphene oxide nanosheets*. Arabian Journal of Chemistry, 2020. **13**(1): p. 2659-2670.
29. Kargar, M. and G. Zolfaghari, *Hybrid Nano-filtration and Micro-filtration Pilot Processes for the Removal of Chromium from Water*. Journal of Water and Wastewater, 2018. **29**(5).
30. Khanzada, Z.T., *Phosphorus Removal from Landfill Leachate by Microalgae*. Biotechnology Reports, 2020: p. e00419.
31. Beluci, N.d.C.L., et al., *Hybrid treatment of coagulation/flocculation process followed by ultrafiltration in TiO<sub>2</sub>-modified membranes to improve the removal of reactive black 5 dye*. Science of the Total Environment, 2019. **664**: p. 222-229.
32. Jia, P., et al., *Cyanobacterium removal and control of algal organic matter (AOM) release by UV/H<sub>2</sub>O<sub>2</sub> pre-oxidation enhanced Fe (II) coagulation*. Water research, 2018. **131**: p. 122-130.
33. Bulgariu, L. and D. Bulgariu, *Functionalized soy waste biomass-A novel environmental-friendly biosorbent for the removal of heavy metals from aqueous solution*. Journal of Cleaner Production, 2018. **197**: p. 875-885.
34. Liang, X., et al., *Efficient removal of Cr (VI) from water by quaternized chitin/branched polyethylenimine biosorbent with hierarchical pore structure*. Bioresource technology, 2018. **250**: p. 178-184.
35. Pradhan, D., et al., *Biosorption for removal of hexavalent chromium using microalgae Scenedesmus sp.* Journal of cleaner production, 2019. **209**: p. 617-629.
36. Wang, G., et al., *Removal of Pb (II) from aqueous solutions by Phytolacca americana L. biomass as a low cost biosorbent*. Arabian Journal of Chemistry, 2018. **11**(1): p. 99-110.
37. Efome, J.E., et al., *Insight studies on metal-organic framework nanofibrous membrane adsorption and activation for heavy metal ions removal from aqueous solution*. ACS applied materials & interfaces, 2018. **10**(22): p. 18619-18629.

38. Hayati, B., et al., *Heavy metal adsorption using PAMAM/CNT nanocomposite from aqueous solution in batch and continuous fixed bed systems*. Chemical Engineering Journal, 2018. **346**: p. 258-270.
39. Kazantsev, S., et al., *Effect of the Morphology of  $\gamma$ -Al<sub>2</sub>O<sub>3</sub> Nanosized Particles on Their Adsorption Properties*. Russian Journal of Physical Chemistry A, 2020. **94**: p. 806-809.
40. Khandare, D. and S. Mukherjee, *A Review of Metal oxide Nanomaterials for Fluoride decontamination from Water Environment*. Materials Today: Proceedings, 2019. **18**: p. 1146-1155.
41. Liu, W., et al., *Nano-sized plate-like alumina synthesis via solution combustion*. Ceramics International, 2019. **45**(8): p. 9919-9925.
42. Dhawale, V.P., V. Khobragade, and S.D. Kulkarni, *Synthesis and Characterization of Aluminium Oxide (Al<sub>2</sub>O<sub>3</sub>) Nanoparticles and its Application in Azodye Decolourisation*. chemistry, 2018. **27**: p. 31.
43. Farahmandjou, M. and N. Golabiyan, *Synthesis and characterisation of Al<sub>2</sub>O<sub>3</sub> nanoparticles as catalyst prepared by polymer co-precipitation method*. Materials Engineering Research, 2019. **1**(2): p. 40-44.
44. Subbotin, D., et al. *Plasma synthesis of Al<sub>2</sub>O<sub>3</sub> from related nitrate*. in *Journal of Physics: Conference Series*. 2018. IOP Publishing.
45. Tabesh, S., F. Davar, and M.R. Loghman-Estarki, *Preparation of  $\gamma$ -Al<sub>2</sub>O<sub>3</sub> nanoparticles using modified sol-gel method and its use for the adsorption of lead and cadmium ions*. Journal of Alloys and Compounds, 2018. **730**: p. 441-449.
46. Varghese, N., et al., *PVA-assisted synthesis and characterization of nano  $\alpha$ -alumina*. 2014.
47. Fumo, D., M. Morelli, and A. Segadaes, *Combustion synthesis of calcium aluminates*. Materials Research Bulletin, 1996. **31**(10): p. 1243-1255.
48. Nassar, M.Y., I.S. Ahmed, and I. Samir, *A novel synthetic route for magnesium aluminate (MgAl<sub>2</sub>O<sub>4</sub>) nanoparticles using sol-gel auto combustion method and their photocatalytic properties*. Spectrochimica Acta Part A: Molecular and Biomolecular Spectroscopy, 2014. **131**: p. 329-334.
49. Nassar, M.Y., et al., *MgO nanostructure via a sol-gel combustion synthesis method using different fuels: An efficient nano-adsorbent for the removal of some anionic textile dyes*. Journal of Molecular Liquids, 2017. **225**: p. 730-740.
50. Varma, A., et al., *Combustion synthesis of advanced materials: principles and applications*, in *Advances in chemical engineering*. 1998, Elsevier. p. 79-226.
51. Ye, T., et al., *Combustion synthesis and photoluminescence of nanocrystalline Y<sub>2</sub>O<sub>3</sub>: Eu phosphors*. Materials Research Bulletin, 1997. **32**(5): p. 501-506.
52. Dru, D., et al., *Conductive Polymer Grafting Platinum Nanoparticles as Efficient Catalysts for the Oxygen Reduction Reaction: Influence of the Polymer Structure*. Electrocatalysis, 2018. **9**(5): p. 640-651.
53. Xing, S., et al., *Highly controlled core/shell structures: tunable conductive polymer shells on gold nanoparticles and nanochains*. Journal of Materials Chemistry, 2009. **19**(20): p. 3286-3291.
54. Yang, J., et al., *Effective removal of heavy metals by nanosized hydrous zirconia composite hydrogel and adsorption behavior study*. Environmental Science and Pollution Research, 2018. **25**(33): p. 33464-33477.
55. Zhao, W., et al., *Molecularly imprinted polymeric nanoparticles decorated with Au NPs for highly sensitive and selective glucose detection*. Biosensors and Bioelectronics, 2018. **100**: p. 497-503.
56. Moon, J.-M., et al., *Conducting polymer-based electrochemical biosensors for neurotransmitters: A review*. Biosensors and Bioelectronics, 2018. **102**: p. 540-552.
57. Brandt, J., *Screening new emerging flame retardant technology in various polymer matrices*. 2018.

58. Zhang, X., et al., *Flame-retardant, highly sensitive strain sensors enabled by renewable phytic acid-doped biotemplate synthesis and spirally structure design*. Chemical Engineering Journal, 2019. **374**: p. 730-737.
59. Kausar, A., *Potential of Polymer/Graphene Nanocomposite in Electronics*. American Journal of Nanoscience and Nanotechnology Research, 2018. **6**(1): p. 55-63.
60. Panda, S. and B. Acharya. *Electronic applications of conducting polymer nanocomposites*. in *Proceedings of the Third International Conference on Microelectronics, Computing and Communication Systems*. 2019. Springer.
61. Hu, Q., et al., *Intracellular polymer substances induced conductive polyaniline for improved methane production from anaerobic wastewater treatment*. ACS Sustainable Chemistry & Engineering, 2019. **7**(6): p. 5912-5920.
62. Zare, E.N., A. Motahari, and M. Sillanpää, *Nanoadsorbents based on conducting polymer nanocomposites with main focus on polyaniline and its derivatives for removal of heavy metal ions/dyes: a review*. Environmental research, 2018. **162**: p. 173-195.
63. Che, Y., et al., *"On Water" Surface-initiated Polymerization of Hydrophobic Monomers*. Angewandte Chemie International Edition, 2018. **57**(50): p. 16380-16384.
64. Singh, V., et al., *Non-specific adsorption of serum and cell lysate on 3D biosensor platforms: A comparative study based on SPRI*. Arabian Journal of Chemistry, 2019. **12**(8): p. 3038-3045.
65. Yongabi, D., et al., *Cell detection by surface imprinted polymers SIPs: A study to unravel the recognition mechanisms*. Sensors and Actuators B: Chemical, 2018. **255**: p. 907-917.
66. Zhang, Z., et al., *A comparative study on grafting polymers from cellulose nanocrystals via surface-initiated atom transfer radical polymerization (ATRP) and activator re-generated by electron transfer ATRP*. Carbohydrate polymers, 2019. **205**: p. 322-329.
67. Frikha, K., et al., *Elaboration of alumina-based materials by solution combustion synthesis: A review*. Comptes Rendus Chimie, 2019. **22**(2): p. 206-219.
68. Kishan, J., et al., *Aqueous combustion synthesis and characterization of zirconia–alumina nanocomposites*. Journal of Alloys and Compounds, 2010. **490**(1): p. 631-636.
69. Nassar, M.Y. and E.A. Abdelrahman, *Hydrothermal tuning of the morphology and crystallite size of zeolite nanostructures for simultaneous adsorption and photocatalytic degradation of methylene blue dye*. Journal of Molecular Liquids, 2017. **242**: p. 364-374.
70. Prabhakar, R. and S.R. Samadder, *Low cost and easy synthesis of aluminium oxide nanoparticles for arsenite removal from groundwater: A complete batch study*. Journal of Molecular Liquids, 2018. **250**: p. 192-201.
71. Li, T., et al., *Synthesis of graphene/polyaniline copolymer for solid-state supercapacitor*. Journal of Electroanalytical Chemistry, 2020. **860**: p. 113908.
72. Singh, A.K., et al., *Electronic properties of soluble functionalized polyaniline (polyanthranilic acid)-multiwalled carbon nanotube nanocomposites: Influence of synthesis methods*. Synthetic Metals, 2011. **161**(5): p. 481-488.
73. Trchová, M., et al., *Conducting polyaniline prepared in the solutions of formic acid: Does functionalization with carboxyl groups occur?* Spectrochimica Acta Part A: Molecular and Biomolecular Spectroscopy, 2020. **235**: p. 118300.
74. Li, L.-L., et al., *One-step synthesis of self-healable hydrogels by the spontaneous phase separation of linear multi-block copolymers during the emulsion copolymerization*. Chinese Chemical Letters, 2017. **28**(4): p. 868-874.
75. Liu, Z. and Q. Wang, *Radical coupling copolymerization (RCCP) for synthesis of various polymers*. Polymer, 2016. **100**: p. 56-59.
76. Qiang, P., et al., *Electron-deficient 1,2,7,8-tetraazaperylene derivative: Efficient synthesis and copolymerization*. European Polymer Journal, 2018. **107**: p. 67-73.

77. Li, S., *Combustion synthesis of porous MgO and its adsorption properties*. International Journal of Industrial Chemistry, 2019. **10**(1): p. 89-96.
78. Gao, Y., et al., *Synthesis of ordered mesoporous La<sub>2</sub>O<sub>3</sub>-ZrO<sub>2</sub> composites with encapsulated Pt NPs and the effect of La-doping on catalytic activity*. Journal of Colloid and Interface Science, 2017. **503**: p. 178-185.
79. Li, M., et al., *Highly selective adsorption of vanadium (V) by nano-hydrous zirconium oxide-modified anion exchange resin*. Journal of Hazardous Materials, 2020. **384**: p. 121386.
80. Li, W., et al., *Comparison of ion exchange and solvent extraction in recovering vanadium from sulfuric acid leach solutions of stone coal*. Hydrometallurgy, 2013. **131-132**: p. 1-7.
81. Hu, D. and L. Wang, *Adsorption of amoxicillin onto quaternized cellulose from flax noil: Kinetic, equilibrium and thermodynamic study*. Journal of the Taiwan Institute of Chemical Engineers, 2016. **64**: p. 227-234.
82. Nassar, M.Y., I.S. Ahmed, and M.A. Raya, *A facile and tunable approach for synthesis of pure silica nanostructures from rice husk for the removal of ciprofloxacin drug from polluted aqueous solutions*. Journal of Molecular Liquids, 2019. **282**: p. 251-263.
83. Ho, Y.-S., *Second-order kinetic model for the sorption of cadmium onto tree fern: A comparison of linear and non-linear methods*. Water Research, 2006. **40**(1): p. 119-125.
84. Batzias, F.A. and D.K. Sidiras, *Dye adsorption by prehydrolysed beech sawdust in batch and fixed-bed systems*. Bioresource Technology, 2007. **98**(6): p. 1208-1217.
85. Muthukumar, C., V.M. Sivakumar, and M. Thirumarimurugan, *Adsorption isotherms and kinetic studies of crystal violet dye removal from aqueous solution using surfactant modified magnetic nanoadsorbent*. Journal of the Taiwan Institute of Chemical Engineers, 2016. **63**: p. 354-362.
86. Agarwal, S., et al., *Synthesis and characteristics of polyaniline/zirconium oxide conductive nanocomposite for dye adsorption application*. Journal of Molecular Liquids, 2016. **218**: p. 494-498.
87. Hashemian, S., M.K. Ardakani, and H. Salehifar, *Kinetics and thermodynamics of adsorption methylene blue onto tea waste/CuFe<sub>2</sub>O<sub>4</sub> composite*. 2013.
88. Cui, H., et al., *Thermotolerance and Antibacterial Properties of MgO-Triclosan Nanocomposites*. Procedia Engineering, 2015. **102**: p. 410-416.
89. Venkatesha, T.G., et al., *Kinetics and thermodynamics of reactive and vat dyes adsorption on MgO nanoparticles*. Chemical Engineering Journal, 2012. **198-199**: p. 1-10.
90. Liu, S., et al., *Adsorption of the anionic dye Congo red from aqueous solution onto natural zeolites modified with N,N-dimethyl dehydroabietylamine oxide*. Chemical Engineering Journal, 2014. **248**: p. 135-144.